Materials Science and Engineering, Volume 46, No. 1 (2021), pp. 5–13.
http://doi.org/10.32974/mse.2021.001

PARTICULATE MATTER CONCENTRATION SENSING IN A METALWORKING WORKSHOP

CSONGOR BÁTHORY[1] – ZSOLT DOBÓ[2] – ÁRPÁD BENCE PALOTÁS[3]

Abstract: One of the most common indoor air pollutants is particulate matter, which was measured in a metalworking workplace for three days at different operation capacities. These preliminary measurements were performed to describe the typical pollution levels of the specified workplace. Air quality limits at workplaces refer to an 8-hour average, so an on the fly calculation method was tested to predict the average concentration. Based on the measured and calculated information, a three-stage light indicated the level of air pollution. Additionally, the possibilities of reducing air pollution were defined.

Keywords: sensor, PM10, air quality

INTRODUCTION

There is an increasing interest in outdoor dust pollution [1–12], but in order to protect human health, we must not forget the importance of indoor air quality, including the workplaces [13–16]. With the spread of low-cost sensory measurement technology, it has become available to sense the air quality in our homes or workplaces. Workplace air can be loaded from several sources by gaseous and solid pollutants. The concentration measurement of particulate matter was performed for three working days in a metalworking workshop using a measuring device with a microcontroller-based particulate matter sensor. The possibility of how it can contribute to the improvement of air quality was investigated.

1. MATERIALS AND METHODS

1.1. Measuring device

A microcontroller-based measuring device containing PMS7003 low-cost sensor was utilized for indoor air pollution measurement. The general layout has already been published in another study [17]. In addition to the measurement of particulate matter, the temperature, humidity, and pressure values were measured by a BME680

[1] Department of Combustion Technology and Thermal Energy, University of Miskolc
H-3515 Miskolc-Egyetemváros, Hungary
csongor.bathory@uni-miskolc.hu
[2] Department of Combustion Technology and Thermal Energy, University of Miskolc
H-3515 Miskolc-Egyetemváros, Hungary
zsolt.dobo@uni-miskolc.hu
[3] Department of Combustion Technology and Thermal Energy, University of Miskolc
H-3515 Miskolc-Egyetemváros, Hungary
zsolt.dobo@uni-miskolc.hu

sensor. An Arduino Nano microcontroller controlled the operation of the sensors and processes the gathered data. To record time and save timestamps to an SD card, a DS3231 based real-time clock was also connected to the microcontroller. A three-stage coloured lamp indicator was added to the measuring device to indicate the concentration level of the particulate matter during the measurement. The green, yellow, and red indicator lights switched through IRF510 transistors by the microcontroller. The indicator light operated at 12 V, the Arduino, PMS7003 and microSD card reader operated at 5 V, while the BME680 and DS3231 at 3.3 V. The schematic drawing of the measuring device, including the above-mentioned components, is shown in *Figure 1*.

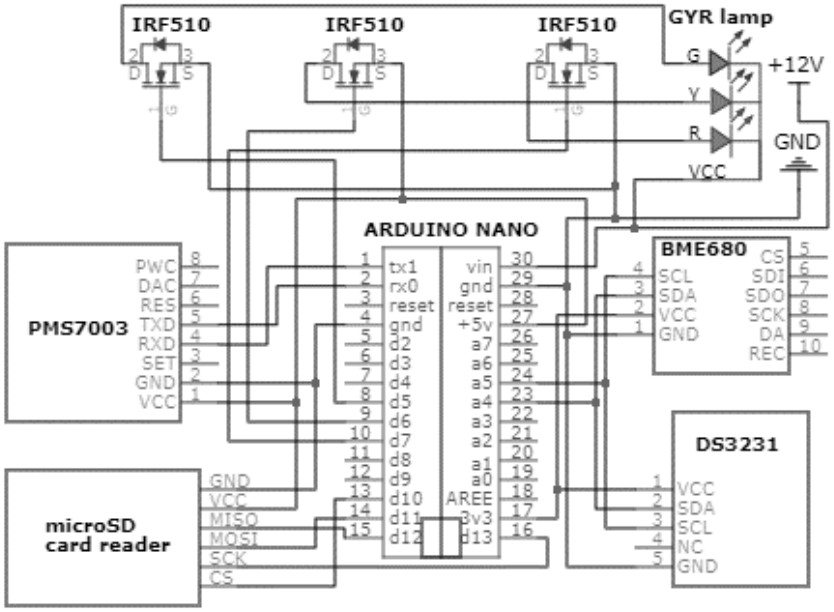

Figure 1
Schematic drawing of measuring device

The sensors were placed in lamellated housing for proper airflow and protection from direct physical impact. The lamp was placed above the lamellar layers, and the other components were placed in a lower sealed box. The box and lamella parts were printed with a 3D printer using PETG material.

1.2. Calibration method

The particulate matter sensor has been calibrated to improve the data quality and accuracy. Taking into account the study of Sayahi et al. [18], the measuring device equipped with a particulate matter sensor was placed in a climate chamber in order to control the environmental parameters. The climate chamber used in this study creates stable environmental parameters in the interior space of about 850 × 850 × 850

mm. Based on preliminary flow tests, the measuring device and the factory-calibrated TSI Dusttrack (TSI) dust aerosol monitor as a reference was placed in the upper 1/3 of the chamber, because there were the most stable temperature, humidity and flow conditions.

Soot from the combustion of isobutene gas was passed through the observation opening of the climate chamber by a fan, thus increasing the concentration of particulate matter inside. The decrease of the elevated PM_{10} (the concentration of particulate matter below 10 µm in diameter) concentration was recorded with the measuring device and the TSI reference.

Figure 2 shows the relationship between the PM_{10} concentrations measured by the PMS7003 and the TSI (circle). The calibration function determined from that can be expressed as $y = 0.58 \times x + 0.01$. The calibration result utilizing this equation is also depicted (square). At 95% the confidence interval is calculated to 2.48 µg/m^3.

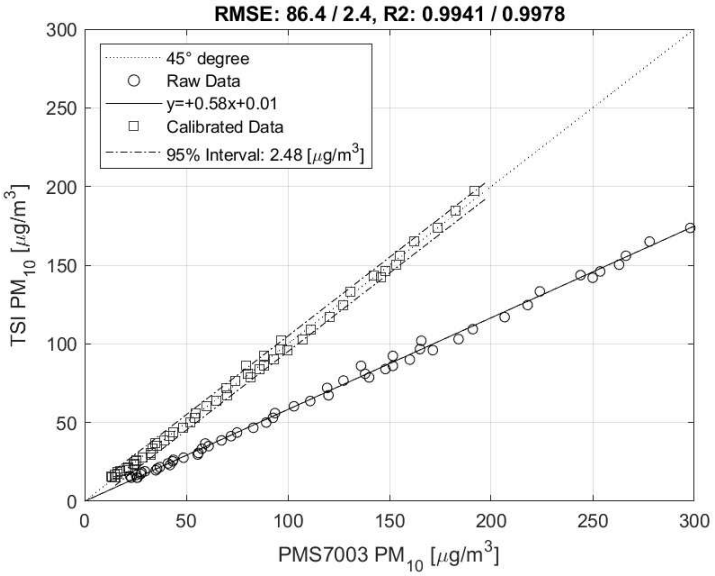

Figure 2
Results of PM_{10} calibration measurements

$PM_{2.5}$ and PM_1 calibrations were made with the same methodology as above. The calibration functions were used during the data processing of the microcontroller, so the already calibrated values were recorded in the work environment.

1.3. Measurement location and time

The measuring device, equipped with a lamp and a calibrated particulate matter sensor, was placed in a metalworking workshop. During the measurements, the main work processes were cutting, turning, and welding. The measuring unit was placed at the inspiratory height (160 cm) equally far from each workstation.

Table 1

Measurement date, duration, and dust generating work operation capacity

No.	Date	Duration	Operation capacity
#1	21. 12. 2020.	6 hour 40 minutes	full
#2	22. 12. 2020.	8 hours 5 minutes	half
#3	23. 12. 2020.	5 hours 34 minutes	zero

Measurements were performed with the installed measuring device on three working days as *Table 1* shows. On the first day, 21 December 2020, the workshop was operating at full capacity, cutting, and welding work was carried out. On the second day, 22 December 2020, they worked on semi capacity, and on the third day, 23 December 2020, no work was carried which usually generates dust. The latter is therefore a baseline and the former are a period of peak and average concentration.

1.4. Threshold concentration

The Hungarian legislation [19] determines the allowable average concentration for particulate matters. The allowable average concentration is the concentration of an air pollutant in the workplace's air which does not normally have an effect on the health of workers. Besides specified particulate matter materials (graphite powder, quartz, etc.) for the other inert powders the allowable average concentration is 10,000 µg/m^3 inhalable concentration (PM_{100}) and 6,000 µg/m^3 respirable concentration (PM_4). The calculation equivalence is the following:

$$C_{avg} = \frac{C_1 * t_1 + C_2 * t_2 + \cdots + C_n * t_n}{t_1 + t_2 + \cdots + t_n}$$

where, C_{avg} is the average concentration and C_1, C_2 … C_n are the concentration for the period t_1, t_2 … t_n, and $t_1+t_2+\ldots+t_n = 8$ hours.

Focusing on the working processes, the allowable concentrations can be stricter. The American Conference of Governmental Industrial Hygienists (ACGIH) recommends a TLV-TWA (Threshold Limit Value-Time Weighted Average) of 5,000 µg/m^3 for total welding fume, assuming that it contains no highly toxic components [20, 21]. Interestingly, the WHO recommends the outdoor 24-hour concentration limit value for PM_{10} as 50 µg/m^3 and for $PM_{2.5}$ as 25 µg/m^3 [22].

1.5. Data processing method

The calibrated minutely mean values of the measuring device were smoothed. The actual value was smoothed based on the weighted values of the past 10 minutes.

Predicted values were calculated using the smoothed values as the expected average concentration value over the entire 8-hour working time, assuming that the particulate matter concentration remains at the current measured value during the remaining period of the working time. Based on the Hungarian legislation calculation equivalence of the predicted average concentration (C_{pred}) is the following:

$$C_{pred} = \frac{C_{elapsed} * t_{elapsed} + C_{present} * t_{remaining}}{t_{elapsed} + t_{remaining}},$$

where $t_{elapsed} + t_{remaining} = 8$ hours.

As the predicted average concentration is calculated on the fly by the microcontroller, the indication light changed the color based on this value to show the relationship to the limit values, allowable average concentration.

2. RESULTS

Data from the three measurement days were evaluated. The first day covers 6 hours and 40 minutes, the second day covers the entire 8 hours of work, and the third day covers 5 hours and 15 minutes.

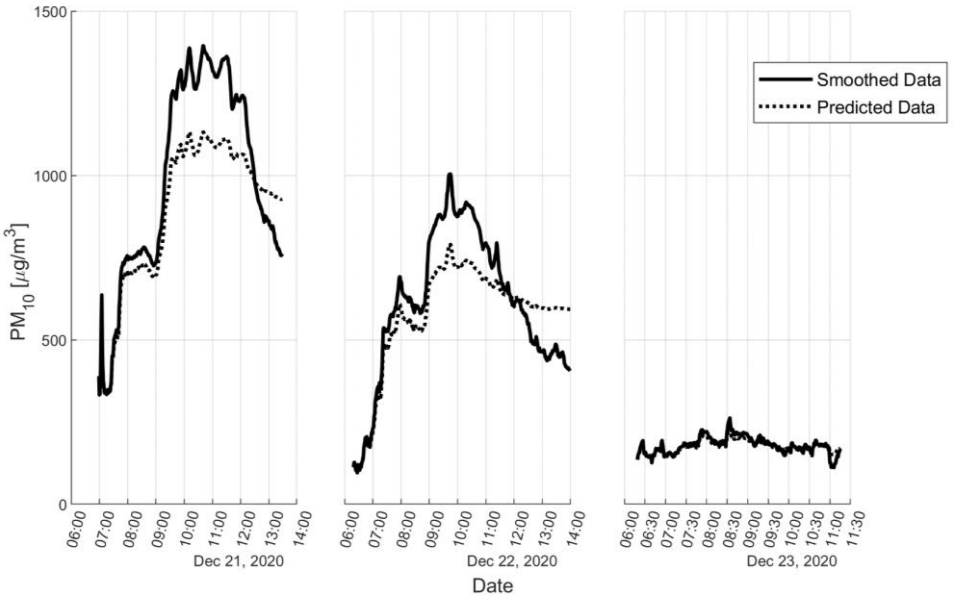

Figure 3

Results of PM_{10} calibration measurements

Figure 3 shows the smoothed and predicted PM_{10} concentrations measured on three days with different operational capacities. On the first day, we can observe that the predicted data show less than the smoothed data in the ascending sections, and then from 12:30 onwards in the decreasing section they show a higher value than the current one. The reason for this is that the predicted values take into account the earlier time intervals, i.e. in this case also the periods where higher concentrations were measured. At the end of the measurement time it indicates the average value for the whole measurement period. At the beginning of the measurement, some outliers are displayed, which may be due to some direct, nearby contamination. On the second

day, the smoothed and predicted data show similar trends as the first day but in lower levels. During the third day concentrations did not increase significantly, so smoothed and predicted values show a similar trend and remain under 300 µg/m^3 throughout the investigated period.

Table 2 shows the maximum, average, and the last predicted PM_{10} concentrations of the three days. Based on the known operation capacity the levels of pollution associated with the characteristic of the shift may be defined. The basic level of pollution is under 200 µg/m^3 average concentration as the operation is zero, the medium level of pollution is under 600 µg/m^3 average concentration and the high level of pollution is over 900 µg/m^3 maximum concentration. The pollution level of an 8-hour shift above is typical just for the investigated metalworking workshop. Based on the defined pollution levels the coloured indicator lamp's operation may be determined with the on the fly calculated predicted concentration.

The average and the last predicted concentrations are different except for the second day, which covers the entire 8-hour period, which supports the correctness of the prediction.

Table 2

Maximum, average and the last predicted PM_{10} concentrations on the three days

No.	Date	C_{max} [µg/m^3]	C_{avg} [µg/m^3]	C_{pred} [µg/m^3]	Pollution level
#1	21. 12. 2020.	1,394.1	962.4	928.4	High
#2	22. 12. 2020.	1,004	586.6	586.7	Medium
#3	23. 12. 2020.	261.9	170.7	170.3	Basic

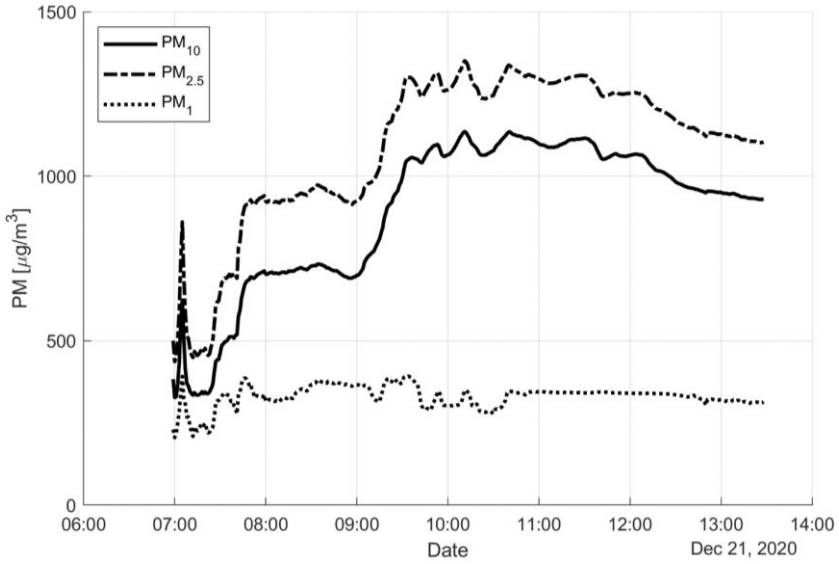

Figure 4

Predicted PM concentration on 21. 12. 2020

Figure 4 shows the predicted concentration of PM_{10}, $PM_{2,5}$ and PM_1 on 21. 12. 2020, which was a day with a high pollution level. Due to their definition, the highest values are the PM_{10} values. The allowable average concentration level was not reached by any PM component on any day. The indicator lights can glow green, yellow or red in individual ways, depending on the concentration levels found in the workplace.

CONCLUSION

The low-cost sensor based measuring device equipped with a microcontroller and an internal clock operated without failure during the three measurement days and recorded the data with a time stamp. Measured data were smoothed and predicted on the fly. Smoothed data shows the actual concentrations. This information can be useful to control a ventilation system and allows for quick intervention to reduce the pollution level. The predicted values illustrate the expected particulate matter load over the entire working time and show the average of the actual 8 hours by the end of the day. The three different operation capacity of the days defined the three levels of pollution of the metalworking workshop. The indicator lights should be programmed based on the predicted data. If the data reache the defined pollution levels the lights can immediately show the workers the expected air load for the full-time work period. From the predicted data, the last value of the working time is recommended for long-term observations, so the 8-hour average values measured on each working day can be fed into the company's monitoring system and can be tracked by the environmental officer. A Wi-Fi module installation is recommended to solve the data transfer. Thanks to the protective housing, the measuring device can also be used in industrial environments, and the digital output of the Arduino can be connected to the ventilation controller to keep the particulate matter concentration at a lower level in the workplace.

ACKNOWLEDGEMENT

Supported by the ÚNKP-20-3 New National Excellence Program of the Ministry for Innovation and Technology from the source of the National Research, Development and Innovation Fund.

REFERENCES

[1] Nieckarz, Z., Zoladz, J. A. (2020). Low-cost air pollution monitoring system — an opportunity for reducing the health risk associated with physical activity in polluted air. *PeerJ*, Vol. 8, p. e10041, http://doi.org/10.7717/peerj.10041.

[2] Beelen, R., Stafoggia, M., Raaschou-Nielsen, O., Andersen, Z. J., Xun, W. W., Katsouyanni, K. et al. (2014). Long-term exposure to air pollution and cardiovascular mortality: an analysis of 22 European cohorts. *Epidemiology*, pp. 368–378, http://doi.org/10.1097/EDE.0000000000000076.

[3] Provost, E. B., Louwies, T., Cox, B., Op‘t Roodt, J., Solmi, F., Dons, E. et al. (2016). Short-term fluctuations in personal black carbon exposure are associated with rapid changes in carotid arterial stiffening. *Environment international*, Vol. 88, pp. 228–234, http://doi.org/10.1016/j.envint.2015.12.023.

[4] Valavanidis, A., Fiotakis, K., Vlachogianni, T. (2008). Airborne particulate matter and human health: toxicological assessment and importance of size and composition of particles for oxidative damage and carcinogenic mechanisms. *Journal of Environmental Science and Health*, Part C, Vol. 26, pp. 339–362, http://doi.org/10.1080/10590500802494538.

[5] Wu, J., Cheng, W., Lu, H., Shi, Y., He, Y. (2018). The Effect of Particulate Matter on Visibility in Hangzhou, China. *Journal of Environmental Science and Management*, Vol. 21, pp. 100–109.

[6] Jolliet, O., Antón, A., Boulay, A.-M., Cherubini, F., Fantke, P., Levasseur, A. et al. (2018). Global guidance on environmental life cycle impact assessment indicators: impacts of climate change, fine particulate matter formation, water consumption and land use. *The International Journal of Life Cycle Assessment*, Vol. 23, pp. 1–19, http://doi.org/10.1007/s11367-018-1443-y.

[7] He, H., Liang, X. Z., Wuebbles, D. J. (2018). Effects of emissions change, climate change and long-range transport on regional modeling of future US particulate matter pollution and speciation. *Atmospheric Environment*, Vol. 179, pp. 166–176, http://doi.org/10.1016/j.atmosenv.2018.02.020.

[8] Jimoda, L. (2012). Effects of particulate matter on human health, the ecosystem, climate and materials: a review. *Facta universitatis-series: Working and Living Enviromental Protection*, Vol. 9, pp. 27–44.

[9] Brook, R. D., Rajagopalan, S., Pope, C. A., Brook, J. R., Bhatnagar, A., Diez-Roux, A. V. et al. (2010). Particulate matter air pollution and cardiovascular disease: an update to the scientific statement from the American Heart Association. *Circulation*, Vol. 121, pp. 2331–2378, http://doi.org/10.1161/cir.0b013e3181dbece1.

[10] Lepeule, J., Laden, F., Dockery, D., Schwartz, J. (2012). Chronic exposure to fine particles and mortality: an extended follow-up of the Harvard Six Cities study from 1974 to 2009. *Environmental health perspectives*, Vol. 120, pp. 965–70, http://doi.org/10.1289/ehp.1104660.

[11] Peters, A., Liu, E., Verrier, R. L., Schwartz, J., Gold, D. R., Mittleman, M. et al. (2000). Air pollution and incidence of cardiac arrhythmia. *Epidemiology*, Vol. 11, pp. 11–17, http://doi.org/10.1097/00001648-200001000-00005.

[12] Pope III, C. A., Burnett, R. T., Thun, M. J., Calle, E. E., Krewski, D., Ito, K. et al. (2002). Lung cancer, cardiopulmonary mortality, and long-term exposure to fine particulate air pollution. *Jama*, Vol. 287, pp. 1132–1141, http://doi.org/10.1001/jama.287.9.1132.

[13] Berlinger, B., Skogen, U., Meijer, C., Thomassen, Y. (2019). Workplace exposure to particulate matter, bio-accessible, and non-soluble metal compounds during hot work processes. *Journal of occupational and environmental hygiene*, Vol. 16, pp. 378–386, http://doi.org/10.1080/15459624.2019.1594841.

[14] Lowther, S. D., Jones, K. C., Wang, X., Whyatt, J. D., Wild, O., Booker, D. (2019). Particulate matter measurement indoors: A review of metrics, sensors, needs, and applications. *Environmental science & technology*, Vol. 53, pp. 11644–11656, http://doi.org/10.1021/acs.est.9b03425.

[15] Stege, T., Bolte, J. F., Claassen, L., Timmermans, D. R. (2020). Development and usability of educational material about workplace particulate matter exposure. *BMC Public Health*, Vol. 21, Article number: 198, http://doi.org/10.1186/s12889-021-10197-x.

[16] Nezis, I., Biskos, G., Eleftheriadis, K., Kalantzi, O.-I. (2019). Particulate matter and health effects in offices-A review. *Building and Environment*, Vol. 156, pp. 62–73, http://doi.org/10.1016/j.buildenv.2019.03.042.

[17] Báthory, C., Palotas, A. B. (2019). Hotspot identification with portable low-cost particulate matter sensor. *International Journal of Energy Water Food Nexus*, Vol. 1, pp. 13–17.

[18] Sayahi, T., Kaufman, D., Becnel, T., Kaur, K., Butterfield, A., Collingwood, S. et al. (2019). Development of a calibration chamber to evaluate the performance of low-cost particulate matter sensors. *Environmental Pollution*, Vol. 255, p. 113131, http://doi.org/10.1016/j.envpol.2019.113131.

[19] 5/2020. (II. 6.) *ITM decree to protect the health and safety of workers exposed to chemical agents*. 2020.

[20] Golbabaei, F., Khadem, M. (2015). Air pollution in welding processes — Assessment and control methods. *Current Air Quality Issues*, pp. 33–63, http://doi.org/10.5772/59793.

[21] ACGIH (2020). Threshold limit values for chemical substances and physical agents and biological exposure indices. United States, Cincinnati: *American Conference of Governmental Industrial Hygienists*, ISBN: 978-1-607261-12-4

[22] WHO (2006). *Air Quality Guidelines: Global Update 2005. Particulate Matter, Ozone, Nitrogen Dioxide and Sulfur Dioxide*. Germany: World Health Organization, ISBN: 92-890-2192-6.

Materials Science and Engineering, Volume 46, No. 1 (2021), pp. 14–23.
http://doi.org/10.32974/mse.2021.002

DISTRIBUTION OF METALS WITHIN DIFFERENT PLANT PARTS OF BIOMASS GATHERED FROM A BROWNFIELD LAND LOCATED IN GYÖNGYÖSOROSZI, HUNGARY

TRUONG PHI DINH[1] – HELGA KOVÁCS[2] – ZSOLT DOBÓ[3]

Abstract: The development of modern technologies requests increasing demand for rare earth elements (REEs) and noble metals (NMs). That has spurred mining activities and has released metals into the environment as a consequence. Phytoextraction uses plants to accumulate metals into their shoots enabling metal removal from brownfields (phytoremediation) or recovery of valuable metals (phytomining). Nevertheless, the occurrence and distribution of NMs, REEs in biomass coming from contaminated lands have not been intensively investigated yet.

In this study, different types of woody biomass including root, trunk, branches, and leaf were collected from a metal-polluted location in Gyöngyösoroszi, Hungary. Afterward, the harvested plants were combusted at 500 °C to generate ashes for ICP (Inductively Coupled Plasma) analysis. Elemental analytical results show that a couple of NMs such as Ag, Au, Pt were found and distributed differently in various biomass ash samples. In specific, the highest Ag concentration is around 5.4 mg/kg achieved in the root ash. Meanwhile, the greatest number of Au and Pt is about 1.8 mg/kg obtained in the trunk and leaf ash respectively. Besides, several REEs with substantial quantities were identified in the contaminated biomass ashes. The significant results observed in the root ash are approximately 47.8 mg/kg Ce and 30.5 mg/kg Nd. The concentration of REEs in root ash is higher than in the above-ground biomass ash with the decreasing order of root ash, leaf ash, trunk, and branches ash. It can be explained by the distribution of REEs in root or leaf is usually greater than other plant parts. These valuable findings indicate that phytomining is a promising approach for recycling NMs, REEs from soils via plants. Moreover, solid residues obtained from polluted biomass are potential metal resources.

Keywords: Biomass, noble metals, rare earth elements, phytoextraction, phytomining

INTRODUCTION

Nowadays, in the context of industrialization and urbanization, the concentration of metals in soils has been increasing significantly resulting in environmental problems and brownfield lands [1]. According to the reported data, more than one-third of the

[1] Department of Combustion Technology and Thermal Energy, University of Miskolc
H-3515 Miskolc-Egyetemváros, Hungary
truong.dinh@uni-miskolc.hu

[2] Department of Combustion Technology and Thermal Energy, University of Miskolc
H-3515 Miskolc-Egyetemváros, Hungary
helga.kovacs@uni-miskolc.hu

[3] Department of Combustion Technology and Thermal Energy, University of Miskolc
H-3515 Miskolc-Egyetemváros, Hungary
zsolt.dobo@uni-miskolc.hu

global land is polluted [2]. The real number even could be greater than what has been unveiled so far. On the other hand, the growth of metals in soil surface simultaneously provides the opportunity for extracting metals from contaminated areas.

Phytoextraction using plants to accumulate metals from soils for removing metals from brownfields refers to phytoremediation [3]–[5]. Additionally, this technique offers the possibility for exploiting valuable metals from mill tailings, overburdens, low-grade ores, or mineralized soil that is not economic by traditional mining methods referred to as phytomining [6]–[8]. Phytoextraction has been proven as an effective, environmentally friendly, safe, and low-cost soil remediation technology [9]–[11], as well as the potential for recovering metals from secondary resources [12]–[14]. Nonetheless, most studies focus on heavy metals such as Ni, Zn, Cd, etc [15]–[19], meanwhile, less attention has been paid in the case of valuable metals including NMs and REEs [20]–[22]. The presence of NMs and REEs in plants was reported in some studies [6], [23]. Concentrations of these valuable metals have been barely investigated showing disparities between different plant parts. Several investigations have verified that the concentration of NMs in the below-ground part (root) is usually higher than in the above-ground parts (stems, leaves) [21], [24]. On the other hand, other studies have verified the declining REEs concentrations in the order of leaf > root > stem [25], [26].

This research investigates the occurrence and distribution of metals comprising NMs and REEs in ligneous plants gathered from a polluted site. In the whole picture of phytomining, plants used for phytoextraction are combusted, following that NMs, REEs are reclaimed from the solid remains. Before the combustion of contaminated biomass is conducted, analyzing valuable metals in ash samples obtained by ashing polluted biomass is essential. This analysis assists to evaluate the feasibility of the phytomining technique and determine the possibility of the further process of combustion.

1. MATERIAL AND METHOD

The source of the biomass utilized in this study is brownfield land in Gyöngyösoroszi, Hungary. In fact, it is an abandoned mining area where industrial lead and zinc production was operating until 1986. The common ligneous plant species living there are oak, pine, wattle, walnut, birch, poplar, and bushes, etc. Different plant parts comprehending root, trunk, branches, and leaf have been collected. The collected woody biomass was cleaned and washed in the case of root samples. They were left at the laboratory under natural conditions in a few weeks for air drying. Afterward, the collected plants have been dried in the oven at 105 °C for 24 hours. This was followed by two-stages ashing processes in the furnace. In the first stage, the dried samples were heated for 2 hours at 250 °C with a heating rate of 50 °C/h. In the second step, the process was continued under the following conditions: heating rate 50 °C/h up to 500 °C, 4 hours waiting at 500 °C. The operation was run twice to ensure carbon-free ash samples. The ashing temperature of contaminated biomass is based on some published studies [27], [28].

The chemical analysis of ash samples was performed by an individual company in Hungary, using Perkin Elmer Avio 200 inductively coupled plasma-optical emission spectrometer (ICP-OES). For the calibration of the measurement, an ICP-OES inner standard solution (Lutecium) was used. The samples were prepared based on the Hungarian standard MSZ EN 13346:2000. The analytical scale was used for taking 5 g samples for analysis. The preparation was carried out by microwave digestion with a Berghof Speedwave 4 laboratory equipment, using nitric acid (2 ml, 67% concentrated) and hydrochloric acid (6 ml, 36% concentrated) solvents. The digestion and dissolution time were 30 minutes at 180 °C. The solution was filled up to 50 ml with 5% concentrated nitric acid after the filtration process using MN616 filters. The concentration of 38 elements including REEs (Ce, Dy, Er, Eu, Gd, Ho, La, Nd, Pr, Sc, Sm, Tb, Tm, Y, Yb), NMs (Ag, Au, Ir, Os, Pd, Pt, Ru, Rh), and others (Cd, Co, Cr, Fe, Mg, Mn, Mo, Na, Ni, Pb, Th, Ti, U, V, Zn) was assigned to identify due to their essentials, high economic value, or toxicity.

2. RESULT AND DISCUSSION

The ICP spectrometry analysis results regarding metal content (up to 38 elements) in ash samples of different types of biomass namely root, trunk, branches, and leaf collected from the contaminated location are given in two tables corresponding to two metal groups. The first metal group shown in Table 1 summarizes elements that are below the detection limit (BDL) in each sample. It can be seen that several NMs (Ir, Os, Pd, Rh, Ru) belong to this group along with a couple of REEs (Ho, Pr, Tb, Tm) and other metals (Th, U). These metals were not used for further evaluations.

Table 1

Metals below the detection limit in ash samples of gathered polluted biomass

Element		Concentration (mg/kg)			
Symbol	**Name**	**Root ash**	**Trunk ash**	**Branches ash**	**Leaf ash**
Ir	Iridium	*<2**	*<1**	*<1**	*<1**
Os	Osmium	*<1.5**	*<1.5**	*<1.5**	*<1.5**
Pd	Palladium	*<2**	*<1**	*<1**	*<1**
Rh	Rhodium	*<1**	*<1**	*<1**	*<1**
Ru	Ruthenium	*<2**	*<2**	*<2**	*<2**
Ho	Holmium	*<1**	*<0.5**	*<0.5**	*<0.5**
Pr	Praseodymium	*<5**	*<3.5**	*<3.5**	*<3.5**
Tb	Terbium	*<1**	*<1**	*<1**	*<1**
Tm	Thulium	*<0.5**	*<0.5**	*<0.5**	*<0.5**
Th	Thorium	*<6**	*<3**	*<3**	*<3**
U	Uranium	*<10**	*<10**	*<10**	*<10**

* The concentration of the metal is BDL (below the detection limit), which is the limit that the concentration can be differentiated from the background noise.

The second metal group consisting of some NMs (Ag, Au, Pt), REEs (Ce, Dy, Er, Eu, Gd, La, Nd, Sc, Sm, Y, Yb) and others (Cd, Co, Cr, Fe, Mg, Mn, Mo, Na, Ni, Pb, Ti, V, Zn) which are detectable in at least one sample. These elements depicted in *Table 2* were used for further investigations. In each metal group, the concentration magnitudes were colored in the increasing order of green-yellow-red.

A couple of NMs such as Ag, Au, Pt were detected and distributed differently in various biomass ash samples *(Figure 1)*. The highest content was 5.369 mg/kg of Ag achieved in the root ash. The other woody ashes (trunk ash, branches ash) performed the same level of 1 mg/kg Ag. While the maximum concentration of Au obtained in trunk ash was 1.880 mg/kg. Au grade of the others ranges from 0.774 to 1.322 (mg/kg) in an ascending sequence: branches ash < leaf ash < root ash. The measurement also shows a considerable amount of Pt was obtained in the collected biomass ashes; its concentrations were in decreasing order of leaf ash (1.848 mg/kg), trunk ash (1.587 mg/kg), and branches (1.002 mg/kg).

Table 2

The concentration of detectable metals in ash samples of gathered polluted biomass

Element		**Concentration (mg/kg)**			
Symbol	**Name**	**Root ash**	**Trunk ash**	**Branches ash**	**Leaf ash**
Noble metals					
Ag	Silver	5.369	1.000	1.000	*<0.5**
Au	Gold	1.322	1.880	0.774	1.215
Pt	Platinum	*<3**	1.587	1.002	1.848
Rare earth elements					
Ce	Cerium	47.755	3.136	2.991	4.557
Dy	Dysprosium	3.942	*<1**	*<1**	*<1**
Er	Erbium	1.897	*<1**	*<1**	*<1**
Eu	Europium	1.660	*<0.25**	*<0.25**	*<0.25**
Gd	Gadolinium	6.467	*<0.5**	*<0.5**	*<1**
La	Lanthanum	20.938	2.558	2.410	3.732
Nd	Neodymium	30.487	1.384	1.538	2.900
Sc	Scandium	8.168	*<0.2**	*<0.2**	*<0.2**
Sm	Samarium	7.485	*<0.5**	*<0.5**	0.549
Y	Yttrium	19.599	1.000	1.344	3.479
Yb	Ytterbium	1.654	*<0.2**	*<0.2**	*<0.2**

Element		Concentration (mg/kg)			
Symbol	**Name**	**Root ash**	**Trunk ash**	**Branches ash**	**Leaf ash**
Other elements					
Cd	Cadmium	170.898	182.909	79.557	82.590
Co	Cobalt	7.342	2.488	1.811	6.677
Cr	Chromium	14.444	3.082	1.606	4.652
Fe	Iron	29,325.561	690.910	605.501	1,254.860
Mg	Magnesium	18,839.407	22,781.691	21,641.779	24,486.568
Mn	Manganese	1,241.806	955.740	1,028.223	1,249.890
Mo	Molyb-denum	1.773	1.360	2.504	0.576
Na	Sodium	1,092.936	3,134.986	965.733	1,030.830
Ni	Nickel	9.752	2.553	4.210	6.823
Pb	Lead	2,289.551	35.294	20.042	12.430
Ti	Titanium	259.383	16.010	17.426	26.682
V	Vanadium	31.452	*<1**	*<1**	*<1**
Zn	Zinc	27,237.674	6,177.369	6,765.875	8,869.407

* The concentration of the metal is BDL (below the detection limit), which is the limit that the concentration can be differentiated from the background noise.

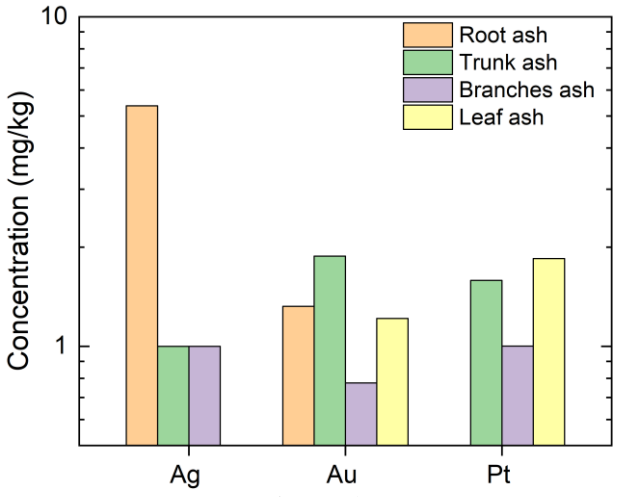

Figure 1

The concentration of NMs in contaminated biomass ash samples

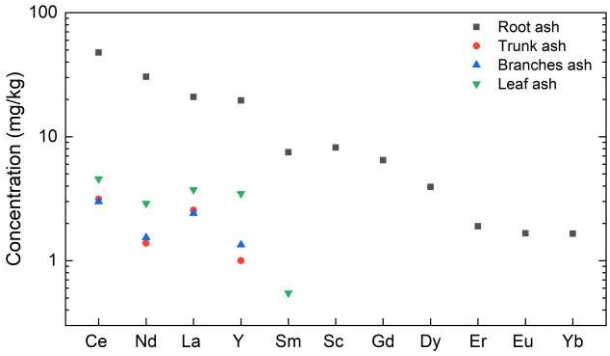

Figure 2

The concentration of REEs in contaminated biomass ash samples

Several REEs with substantial quantities were identified in the contaminated biomass ashes. A few elements comprehending Ce, Nd, La, and Y which presented in all the ash samples. The other metals except Sm were only detectable in the root ash as seen in *Figure 2*. Furthermore, the figure indicates that the concentration of REEs in root ash is higher than in the above-ground biomass ash with the following order: root ash > leaf ash > trunk, branches ash (trunk ash and branches ash performed the same trend). That can be explained by the distribution of REEs in root or leaf is usually higher than other plant parts. The significant results observed in the root ash were 47.755 mg/kg Ce, 30.487 mg/kg Nd, 20.938 mg/kg La, 19.599 mg/kg Y. Meanwhile, REEs were modestly distributed from 0.549 to 4.557 mg/kg in the other samples.

Other elements including heavy metals were also analyzed in this study. Their concentrations varied in a wide range of 0.576 ÷ 29,325.561 mg/kg. The notable findings were 29,325.561 mg/kg Fe and 27,237.674 mg/kg Zn in root ash; 24,486.568 and 22,781.691 mg/kg of Mg in leaf ash and trunk ash respectively. On the basis of Figure 3, to some extent, the contents of these elements in the aerial tissue ash comprising trunk ash, branches ash, leaf ash presented the similarity. It was likely smaller than the concentrations in the root ash (as seen, the dark point mainly above the others).

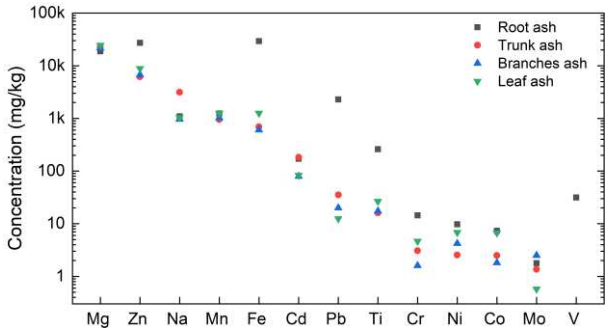

Figure 3

The concentration of other elements in contaminated biomass ash samples

CONCLUSIONS

Chemical analysis results revealed that NMs were detectable in the contaminated biomass ash incinerated at 500 °C. In particular, 5.369 mg/kg of Ag and 1.322 mg/kg of Au were found in the root ash. Meanwhile, in the ash of the trunk Ag, Au and Pt were observed at levels of 1; 1.88; and 1.587 mg/kg respectively. A considerable amount of REEs was identified in the ash samples. The concentration of these elements in the root ash is greater than in the ash of above-ground plant parts in the decreasing order: root ash > leaf ash > trunk, branches ash. This is in complete agreement with the previous studies [29], [30]. Large quantities of other metals including heavy metals were also identified in the polluted biomass ash samples. To some extent, their concentrations performed the similarity in aerial tissue ashes and were likely smaller than the metal contents in the root ash.

The detections of NMs and REEs in the contaminated biomass ashes lay the groundwork and demonstrate the viability of phytomining in recovering valuable metals. In the following stage, the polluted plants will be combusted. Solid remains such as bottom ash, fly ash, deposited ash from different positions in the combustion and flue gas system would be collected and analyzed. Based on the elemental analysis outcomes, further directions would be defined.

ACKNOWLEDGMENT

The research was carried out as part of the *More efficient exploitation and use of subsurface resources* project of the University of Miskolc, implemented in the framework of the Thematic Excellence Program funded by the Ministry of Innovation and Technology of Hungary. (Grant Contract reg. nr.: NKFIH-846-8/2019)

REFERENCES

[1] Alker, S., Joy, V., Roberts, P., Smith, N. (2000). The definition of brownfield. *J. Environ. Plan. Manag.*, Vol. 43, No. 1, pp. 49–69, http://doi.org/10.1080/09640560010766.

[2] Abhilash, P. C., Dubey, R. K., Tripathi, V., Srivastava, P., Verma, J. P., Singh, H. B. (2013). Remediation and management of POPs-contaminated soils in a warming climate: Challenges and perspectives. *Environ. Sci. Pollut. Res.*, Vol. 20, No. 8, pp. 5879–5885, http://doi.org/10.1007/s11356-013-1808-5.

[3] Van Nevel, L., Mertens, J., Oorts, K., Verheyen, K. (2007). Phytoextraction of metals from soils: How far from practice? *Environ. Pollut.*, Vol. 150, No. 1, pp. 34–40, http://doi.org/10.1016/j.envpol.2007.05.024.

[4] Mahar, A. et al. (2016). Challenges and opportunities in the phytoremediation of heavy metals contaminated soils: A review. *Ecotoxicol. Environ. Saf.*, Vol. 126, pp. 111–121, http://doi.org/10.1016/j.ecoenv.2015.12.023.

[5] Yao, Z., Li, J., Xie, H., Yu, C. (2012). Review on Remediation Technologies of Soil Contaminated by Heavy Metals. *Procedia Environmental Sciences*, Vol. 16. pp. 722–729, http://doi.org/10.1016/j.proenv.2012.10.099.

[6] Sheoran, V., Sheoran, A. S., Poonia, P. (2009). Phytomining: A review," *Miner. Eng.*, Vol. 22, No. 12, pp. 1007–1019, http://doi.org/10.1016/j.mineng.2009.04.001.

[7] Chaney, R. L., Baklanov, I. A. (2017). *Phytoremediation and Phytomining*. *Advances in Botanical Research*, Vol. 83,pp. 189–221.

[8] Sheoran, V., Sheoran, A. S., Poonia, P. (2013). Phytomining of gold: A review," *J. Geochemical Explor.*, Vol. 128, pp. 42–50, http://doi.org/10.1016/j.gexplo.2013.01.008.

[9] Chaney, R. L. et al. (1997). Phytoremediation of soil metals. *Curr. Opin. Biotechnol.*, Vol. 8, No. 3, pp. 279–284, Jun., http://doi.org/10.1016/S0958-1669(97)80004-3.

[10] Wan, X., Lei, M., Chen, T. (2016). Cost–benefit calculation of phytoremediation technology for heavy-metal-contaminated soil. *Sci. Total Environ.*, Vol. 563–564, pp. 796–802, http://doi.org/10.1016/j.scitotenv.2015.12.080.

[11] Khan, F. I., Husain, T., Hejazi, R. (2004). An overview and analysis of site remediation technologies. *J. Environ. Manage.*, Vol. 71, No. 2, pp. 95–122, http://doi.org/10.1016/j.jenvman.2004.02.003

[12] Van der Ent, A., Echevarria, G., Baker, A. J. M., Morel, J. L. (eds.) (2018). *Agromining: Farming for Metals*. Cham: Springer International Publishing.

[13] Novo, L. A. B., Castro, P. M. L., Alvarenga, P., da Silva, E. F. (2017). Phytomining of Rare and Valuable Metals. In: Novo, L. A. B., Castro, P. M. L., Alvarenga, P., da Silva, E. F. (eds.) *Phytoremediation*. Cham: Springer International Publishing, pp. 469–486.

[14] Anderson, C., Brooks, R., Stewart, R., Simcock, R., Robinson, B. (1999). The Phytoremediation and Phytomining of Heavy metals. *PACRIM Conference*, pp. 127–135.

[15] van der Ent, A., Baker, A. J. M., Reeves, R. D., Pollard, A. J., Schat, H. (2013). Hyperaccumulators of metal and metalloid trace elements: Facts and fiction. *Plant Soil*, Vol. 362, No. 1–2, pp. 319–334, http://doi.org/10.1007/s11104-012-1287-3.

[16] Anderson, C. W. N. et al. (1999). Phytomining for nickel, thallium and gold. *J. Geochemical Explor.*, Vol. 67, No. 1–3, pp. 407–415, http://doi.org/10.1016/S0375-6742(99)00055-2

[17] Kovacs, H., Bánhidi, O., Veisz, K. (2011). Distribution of chemical elements within ligneous parts of various trees. *Mater. Sci. Eng.*, Vol. 36, pp. 41–50, Jan.

[18] Kovács, H., Paulovics, J., Szemmelveisz, K. (2014). Sustainable reuse of heavy metal contaminated brownfield lands by phytoextraction. *Mater. Sci. Eng.*, Vol. 39, pp. 33–42.

[19] Nicks, L. J., Chambers, M. F. (1998). A pioneering study of the potential of phytomining for nickel. In: *Plants that hyperaccumulate heavy Met. their role phytoremediation, Microbiol. Archaeol. Miner. Explor. phytomining*. R. R. Brooks, Ed. Michigan: CAB International, pp. 313–325.

[20] Anderson, C. W. N., Stewart, R. B., Moreno, F. N., Gardea-torresdey, J. L., Robinson, B. H., Meech, J. (2003). Gold phytomining . Novel Developments in a Plant-based Mining System. *Proc. Gold 2003 Conf. New Ind. Appl. Gold*, No. 2, pp. 35–45.

[21] Msuya, F. A., Brooks, R. R., Anderson, C. W. N. (2000). Chemically-induced uptake of gold by root crops: Its significance for phytomining. *Gold Bull.*, Vol. 33, No. 4, pp. 134–137, http://doi.org/10.1007/BF03215491.

[22] Tyler, G. (2004). Rare earth elements in soil and plant systems – A review. *Plant Soil*, Vol. 267, No. 1–2, pp. 191–206, Dec., http://doi.org/10.1007/s11104-005-4888-2

[23] Liu, C. et al. (2018). *Element Case Studies: Rare Earth Elements*. pp. 471–483. In: A. van der Ent et al. (eds.). *Agromining: Farming for Metals, Mineral Resource Reviews,* Springer International Publishing AG, pp. 297–308, http://doi.org/10.1007/978-3-319-61899-9_19

[24] Feichtmeier, N., Leopold, K. (2015). Bioavailability of Platinum Group Elements to Plants. A Review BT In: *Platinum Metals in the Environment*. Zereini, F., Wiseman, C. L. S. (eds.). Berlin, Heidelberg: Springer Berlin Heidelberg, pp. 311–338.

[25] Miao, L., Ma, Y., Xu, R., Yan, W. (2011). Environmental biogeochemical characteristics of rare earth elements in soil and soil-grown plants of the Hetai goldfield, Guangdong Province, China. *Environ. Earth Sci.*, Vol. 63, No. 3, pp. 501–511, http://doi.org/10.1007/s12665-010-0718-9.

[26] Wang, Y. Q., Sun, J. X., Chen, H. M., Guo, F. Q. (1997). Determination of the contents and distribution characteristics of REE in natural plants by NAA. *J. Radioanal. Nucl. Chem.*, Vol. 219, No. 1, pp. 99–103, May, http://doi.org/10.1007/BF02040273

[27] Krisnayanti, B. D., Anderson, C. W. N., Sukartono, S., Afandi, Y., Suheri, H., Ekawanti, A. (2016). Phytomining for artisanal gold mine tailings management. *Minerals*, Vol. 6, No. 3, pp. 1–11, http://doi.org/10.3390/min6030084.

[28] Lamb, A. E., Anderson, C. W. N., Haverkamp, R. G. (2001). The extraction of gold from plants and its application to phytomining. *Chemistry in New Zealand*, Vol. 65, No. 2, pp. 31–33.

[29] Xu, X., Zhu, W., Wang, Z., Witkamp, G. J. (2002). Distributions of rare earths and heavy metals in field-grown maize after application of rare earth-containing fertilizer. *Sci. Total Environ.*, Vol. 293, No. 1–3, pp. 97–105, http://doi.org/10.1016/s0048-9697(01)01150-0.

[30] Ding, S. M., Liang, T., Yan, J. C., Zhang, Z. L., Huang, Z. C., Xie, Y. N. (2007). Fractionations of rare earth elements in plants and their conceptive model. *Sci. China, Ser. C Life Sci.*, Vol. 50, No. 1, pp. 47–55, http://doi.org/10.1007/s11427-007-2040-7.

Materials Science and Engineering, Volume 46, No. 1 (2021), pp. 24–34.
http://doi.org/10.32974/mse.2021.003

INVESTIGATION OF THE DIFFERENT SAND MIXTURES USING COLD BOX METHOD IN TERMS OF COLLAPSIBILITY

HENRIETTA HUDÁK[1] – KINGA GRASALKOVITS[2] – GÁBOR GYARMATI[3] – IMRE BUDAVÁRI[4] – DÁNIEL MOLNÁR[5] – LÁSZLÓ VARGA[6]

Abstract: Expendable sand cores have to meet several criteria to be suitable for forming the internal cavities of castings. The main characteristics of cores are the mechanical properties and thermal behavior during thermal loading. In this article, cold box sand mixtures with different binder and hardener content were investigated in terms of bending strength, collapsibility, and thermal distortions. The research was motivated by an industrial problem: during the production of a turbocharger casting, problems with the collapsibility were raised. To study the hardening characteristics-, the retained bending strength, and the thermal behavior of the sand cores containing different amounts of binder and hardener, bending tests, collapsibility tests, and hot-distortion tests were conducted.

Keywords: cold box sand mixtures, binder and hardener content, collapsibility, bending strength test, hot distortion test

INTRODUCTION

During casting production, it is essential from the economic and technological point of view to form the internal cavities of castings that are most often provided by using expendable sand cores. Requirements against the sand cores are twofold, in addition to the sufficient initial-, and final strength, they must also have sufficient thermal strength [1].

[1] Institute of Foundry, University of Miskolc
H-3515 Miskolc-Egyetemváros, Hungary
ontheni@uni-miskolc.hu

[2] Institute of Foundry, University of Miskolc
H-3515 Miskolc-Egyetemváros, Hungary
guci444@gmail.com

[3] Institute of Foundry, University of Miskolc
H-3515 Miskolc-Egyetemváros, Hungary
ontgabor@uni-miskolc.hu

[4] Institute of Foundry, University of Miskolc
H-3515 Miskolc-Egyetemváros, Hungary
ontbudai@uni-miskolc.hu

[5] Institute of Foundry, University of Miskolc
H-3515 Miskolc-Egyetemváros, Hungary
daniel.molnar@uni-miskolc.hu

[6] Institute of Foundry, University of Miskolc
H-3515 Miskolc-Egyetemváros, Hungary
ontvlaci@uni-miskolc.hu

The general requirements for sand cores are as follows:

- sufficient dry strength (i.e. strength in the hardened state) of sand cores containing a low amount of binder according to economic and environmental specifications;
- sufficient hot strength to withstand the erosion and thermomechanical loads induced by the flowing liquid metal during the pouring;
- low gas evolution;
- the applied binder system must have a low amount of harmful substances;
- ease of removability from the casting = good collapsibility;
- good reclaimability [2], [3], [4].

It is very important to apply the right quality and quantity of binder during the coremaking process to coat sand grains and to ensure good cohesion between the sand particles. During casting, sand cores are exposed to the heat of the high-temperature metal, so they must have good thermal stability/thermal resistance to maintain the required dimensional accuracy. However, after the pouring, it is essential that the existing cohesion force between the sand grains is ceased by the burn-out of the binder, thus making it possible to easily remove the sand core from the casting [5], [6].

To investigate the collapsibility of the chemically and inorganically bonded sand cores, several methods are applied. The most common method is the evaluation of the residual strength of the standard sand specimens after the thermal loading in a pre-heated furnace. Earlier studies have shown that the strength of the organically bonded sand cores can be increased under short-term thermal loading since the cross-linking of the binder did not undergo completely in sand cores stored at room temperature. In the case of the phenolic resin bonded cold-box sand cores, a significant decrease in the strength of specimens was observed after 10 minutes of thermal exposure. During the research works, sand specimens were heated at a temperature range of 400–450 °C for different periods of time (2.5, 5, 7.5, 10, 15, 20, 25, 30 minutes) [7], [8].

The present research work was an attempt to provide solution proposals about a collapsibility problem of the cold-box sand cores raised in a foundry. Two sand cores with nearly similar geometry were studied *(Figure 1)*. These cores, also called "snail-shaped sand cores", are used to form the internal cavities of automotive turbochargers.

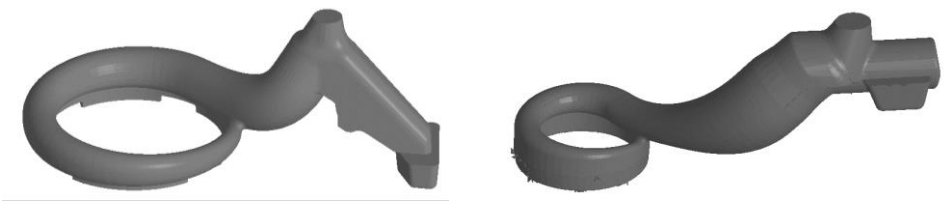

Figure 1
The geometry of sand cores

1. MATERIALS AND METHODS

1.1. Investigated materials

Medium Silica Sand was used as refractory aggregate for producing the standard sand specimens. The quartz sand is characterized by three characteristic grain size fractions: 0.315/0.20/0.16 mm. The foundry sand was sub-rounded shaped with an average grain size 0.22 mm. The measured specific surface area with Blaine method was 122 cm^2/g. The LOI (loss on ignition) of sand samples was 0.1%. *Figure 2* shows the stereomicroscopic image of the quartz sand grains at a magnification of 20×.

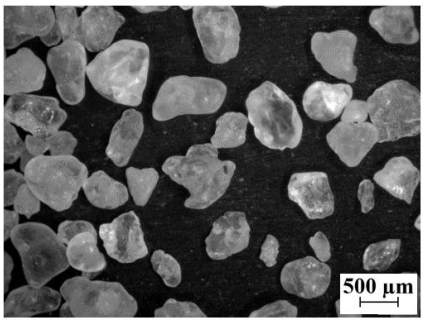

Figure 2
Stereomicroscopic image of the investigated sand at 20× magnification

In the experiments, specimens for the bending tests, collapsibility tests, and hot distortion tests were prepared from polyurethane cold box sand core mixtures containing four different binder-to-hardener ratios. In *Table 1* the compositions of the sand core mixtures are summarized.

Table 1
Composition of the sand core mixtures

	Binder content (based on weight of sand, wt. %)	**Hardener content (based on weight of sand, wt. %)**
1.	0.6	0.4
2.	0.6	0.5
3.	0.6	0.6
4.	0.5	0.5

The sand mixtures were blended using batch sand mixer equipment. 2 kg of quartz sand was used for the preparation of each sand core mixture. First, the hardener (which included the isocyanate component of the binder system) was added to the sand and mixed for 1 minute, followed by the binder, which was blended for an additional 1 minute.

Test specimens were produced from the core mixtures using a Multiserw Morek type core shooting machine. *Table 2* shows the technological parameters that were applied during the cold box coremaking process. These parameters were the same as the operating conditions used in the foundry.

Table 2

The used technological parameters

Shot time [s]	2.0
Amine quantity [ml]	1.5
Time after shot [s]	18
Shot pressure [bar]	6

Figure 3

The Universal Core Shooter by Multiserw-Morek [9] *and three pieces of standard cross-sectioned samples for bending strength test*

1.2. Bending-, and collapsibility tests

The bending test provides a good characterization of the bonding strength of the binder, which connects the sand grains in the specimens. The strength of the sand cores is influenced by several factors: the granulometric-, chemical and thermophysical properties of the foundry sand as well as the amount and quality of the components of the applied binder system [10].

To study the hardening characteristics of the cold box sand cores containing different ratios of the binder and hardener, 3-point bending tests were conducted with a MULTISERW LRu-2e universal strength testing machine *(Figure 4)*. Tests were performed on test bars having dimensions of 22.5 × 22.5 × 180 mm. The bending strength of the specimens was measured immediately after the production of the test bars and after storage times of 1 h, 4 h, and 24 h. The results of the bending strength after 1 h give information about the handling strength of the sand cores. The analysis of storage time with 24 h gives information about the maximum bending strength and storage time of the cold box sand cores.

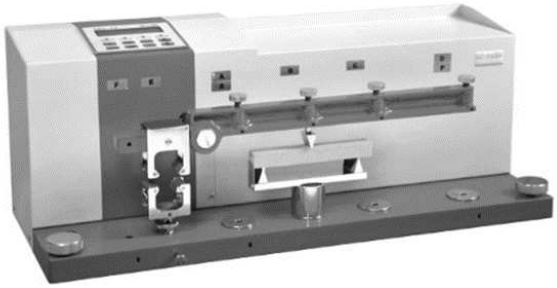

Figure 4
Universal strength testing machine Lru-2e Multiserw-Morek [9]

According to Dietert [11] the retained strength is a good laboratory measure to evaluate the collapsibility of a sand core mixture. For the measurement of the retained strength of specimens, they need to be heated over a range of temperatures in a furnace. After cooling down of the specimens, strength properties can be evaluated. This kind of test can be used for the comparison of different binder types.

During the experiments, bending test bars were produced from cold box sand core mixtures containing different binder and hardener ratios (see Table 1.). Specimens have been stored for 4 h and 24 h then they were placed into a furnace pre-heated up to 400 °C. Test bars were heated for different periods of time (5 min., 7.5 min., 10 min., 12.5 min.) followed by a cooling down period of 1 h. Adoption of the production parameters of previous work of other researchers are used in this work [7], [8]. Bending tests were performed to obtain the retained strength of the specimens.

1.3. Hot distortion test

The hot distortion test gives information about the thermal behavior of the chemically bonded sand cores when they are exposed to heat. Several methods were developed to investigate the hot distortion properties of sand cores [12].

In our experiments, hot distortion tests were conducted using a Simpson Gerosa Hot distortion Tester *(Figure 5).*

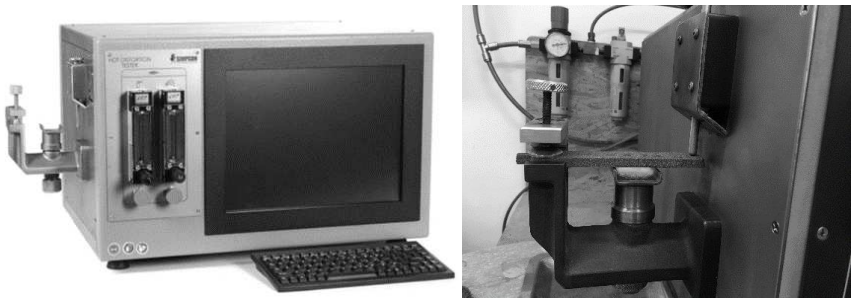

Figure 5
The BCIRA hot distortion tester [14] *and*
the sample holder part of the hot distortion test apparatus

Tests were performed on samples after a storage time of 4 h and 24 h. The technological parameters were adopted from the recent work of other researchers [7]. The specimens dimensions are 114.3 × 25.4 × 6.35 mm [13].

The device measures the deformation and the breakdown time of the specimens when they are exposed to heat [5]. The complete description of the operation of the Hot distortion Tester can be found in the literature [15].

2. RESULTS

2.1. Results of the bending strength test

Figure 6 shows the results of the bending tests.

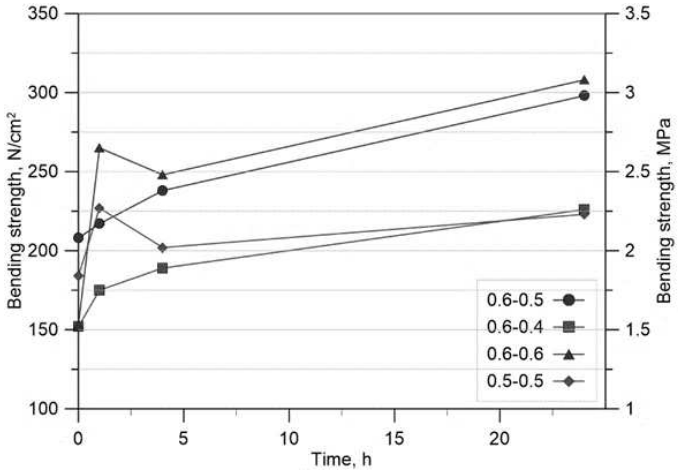

Figure 6

Bending strength test results (immediately, after 1, 4, and 24 hours)

The initial strength of the sand specimens containing 0.6-0.5 binder-hardener ratio was the highest. Despite the initial low strength of the samples with 0.6-0.6 binder-hardener ratio, the bending strength measured after 1 hour was the highest from all of the investigated samples. After a storage time of 4 hours, the strength growth increase, and the bending strength is increasing continuously thereafter during the 24 hour storage time. Interestingly, the shape of the curves (i.e., the hardening characteristics) are similar when the binder and the hardener are used in equal quantities (0.6-0.6 and 0.5-0.5). On the other hand, when the binder is in excess, the curves show continuous hardening without the strength peak at 1 hour. This indicates that the kinetics of hardening are rather sensitive to the applied binder-to-hardener ratio. It can be concluded that the cold box sand cores provide good storage ability.

Results of the collapsibility tests are summarized in *Figure 7* in the case of the specimens stored for 4 hours and *Figure 8* in the case of the samples stored for 24 hours.

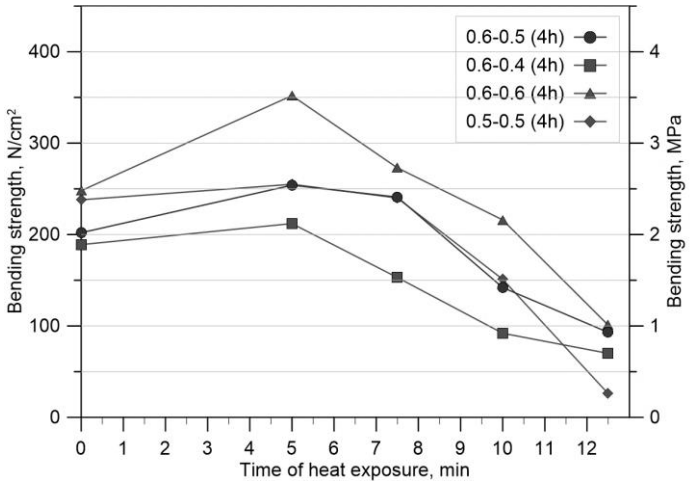

Figure 7

Bending strength test results (heat load; after a storage time of 4 h)

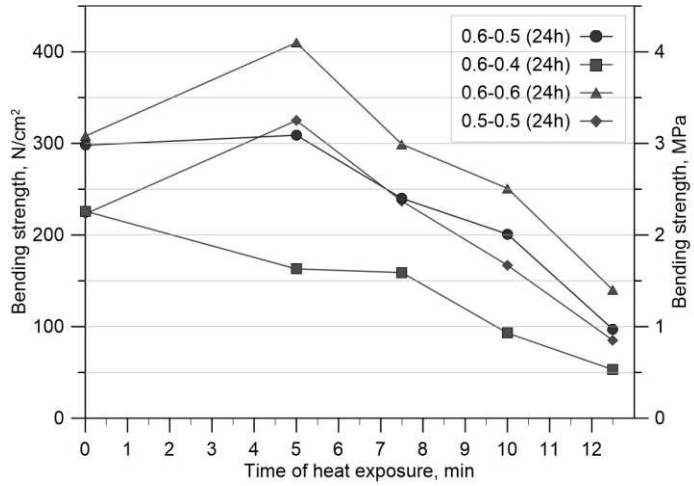

Figure 8

Bending strength test results (heat load; after a storage time of 24 h)

In the case of all sand mixtures, stored for 4 hours and then heated up to 7.5 minutes, an increase in bending strength can be observed. This is caused by the post-curing phenomenon of the organic resin. After the heating time of 7.5 minutes, a continuous decrease in the bending strength of the samples can be found.

Based on the results, the hardener content and the degree of post-curing are proportional to each other. Higher hardener content results in a higher degree of post-curing. When the binder and hardener are used in equal quantities, there is a significant post-curing; while this statement is not valid when there is excess binder in the

system. The post-curing is lesser or even avoided when the binder is in excess, which clearly improves collapsibility.

It can be noticed that except for the specimens characterized with a 0.6-0.4 binder-to-hardener ratio, the bending strength values after heat loading are higher for all mixtures stored for 24 hours. In the case of specimens with a 0.6-0.4 binder-to-hardener ratio, it can be observed that increasing the heating time results in a continuously decreasing retained bending strength of the samples.

Apart from the specimens containing a 0.6-0.4 binder-to-hardener ratio, the bending strength of all samples after heat loading of 7.5 minutes are higher than 200 N/cm^2.

It is important to know that in the foundry where the collapsibility problem of the sand cores was found, the pouring time of the automotive turbochargers is less than 7.5 minutes. From the results of the collapsibility tests, it can be clearly seen that the longer the storage time of the cold box sand cores, the more likely it is that there will be a knock-out problem after casting due to the higher bending strength values.

2.2. Results of the hot distortion tests

Figure 9 shows the hot distortion test results in the case of specimens that have been stored for 4 h, while *Figure 10* presents the results of the hot distortion tests conducted on samples stored for 24 hours.

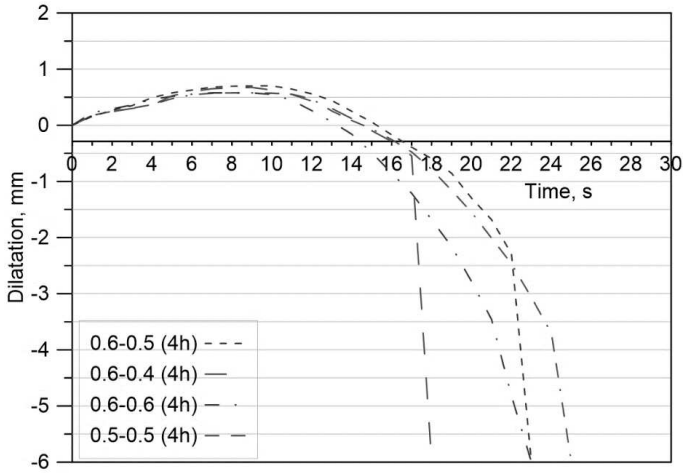

Figure 9

Hot distortion test results (after a storage time of 4 hours)

The results of the performed hot distortion tests show one of the advantages of the cold box coremaking technology. It can provide good dimensional accuracy and dimensional tolerances for the sand cores. From *Figure 9* and *Figure 10*, it can be clearly seen that the cold box sand specimens, exposed to heat during the tests, show good thermal deformation resistance.

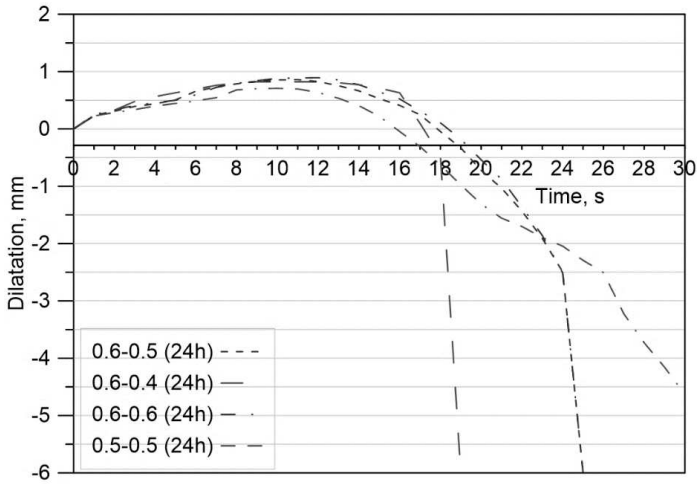

Figure 10
Hot distortion test results (after a storage time of 24 hours)

Maximum deformation of the heated samples is lower than 1 mm. Furthermore, this deformation stage takes place in a very short time (see *Table 3*) The sand specimens containing 0.6-0.5 binder-hardener ratio, which have been stored for 4 hours, show the highest deformation value. The hot distortion test of the specimens that have been stored for 24 hours reflects lower thermal deformation resistance than in the case of the samples stored for 4 hours.

The time of hot distortion tests is relatively short, which shows poor thermal stability of the cold box sand specimens against the heat loading. However, it is essential to note that in some cases, the breakdown failure of the samples was not taken place during the heat loading. Specimens were characterized by plastic deformation. From the results, it can be observed that the higher hardener content resulted in higher degradation time, which results in higher thermal stability in the case of specimens stored for 4 hours. This tendency can also be seen in the case of the specimens that have been stored for 24 hours.

Table 3
Data of the hot distortion test result

Binder-hardener ratio	Max. deformation, mm	Time, s
0.6-0.5 (4h)	0.7014	9
0.6-0.5 (24h)	0.8596	11
0.6-0.4 (4h)	0.6731	9
0.6-0.4 (24h)	0.8221	9
0.6-0.6 (4h)	0.5769	7
0.6-0.6 (24h)	0.8933	12
0.5-0.5 (4h)	0.5769	8
0.5-0.5 (24h)	0.7079	10

By summarizing the results of the hot distortion tests, the more reasonable choice of the four sand core mixtures is, which has a lower tendency of thermal deformation. At the same time, that mixture (0.5-0.5 binder-hardener ratio) has the lowest initial bending strength, which is disadvantageous.

CONCLUSION

Based on the conducted investigations and their results, the following conclusions can be drawn:

1. The binder-to-hardener ratio strongly influences the strength properties, collapsibility, and thermal behavior of the cold box sand cores.
2. By increasing the hardener content, higher bending strength can be achieved, which improves the resistance against the manipulation during the handling process.
3. The performed collapsibility tests show that the increased hardener content results in higher retained bending strength of the sand mixtures, thus making it difficult to remove the sand cores from the castings.
4. The investigated cold box sand specimens are characterized by high thermal deformation resistance and low thermal stability.
5. From the results, it can be concluded that the optimal binder-hardener ratio for producing the turbochargers in the foundry is 0.6-0.5 ratio since it provides sand cores with good initial and final strength as well as moderate retained bending strength after heat loading of the samples.

REFERENCES

[1] Mádi, L. J., Dúl, J., Császár, Cs. (2015). Műgyantás homokmagok szilárdsági tulajdonságainak változása hőterhelés hatására. *The Publications of the MultiScience – XXIX. microCAD International Multidisciplinary Scientific Conference*, April 9–10, 2015, Miskolc, Hungary. University of Miskolc.

[2] Flemming, E., Tilch, W. (1993). *Formstoffe und Formverfahren*. Leipzig, Stuttgart: Deutscher Verlag für Grundstoffindustrie, pp. 37–104.

[3] C. M. Dunks (1971). Cores and Coremaking. In: Castings. J. D. Beadle (ed.), Macmillan Publishers, pp. 49–62.

[4] Beeley, P. (2001). *Foundry Technology*. Butterworth-Heinemann, Oxford, pp. 178–180.

[5] Stauder, B. J., Kerber, H., Schumacher, P. (2016). Foundry sand core property assessment by 3-point bending test evaluation. *Journal of Materials Processing Technology*, 237, pp. 188–196, http://doi.org/10.1016/j.jmatprotec.2016.06.010.

[6] Stauder, B. J., Harmuth, H., Schumacher, P. (2018). De-agglomeration rate of silicate bonded sand cores during core removal. *Journal of Materials Processing Tech.*, 252, pp. 652–658. http://doi.org/10.1016/j.jmatprotec.2017.10.027.

[7] Sipos, L. Á., Fegyverneki, Gy., Budavári, I., Pete, L. G., Varga, L. (2020). Warm-box magkészítési technológiával előállított műgyanta kötésű homokmagok reaktivitásának és üríthetőségi tulajdonságainak vizsgálata. *Bányászati és Kohászati Lapok, Kohászat*, 4/2020, pp. 18–23.

[8] Mádi, L. J., Varga, L., Fegyverneki, Gy., (2016). Műgyantás homokmagok szilárdsági tulajdonságainak változása hőterhelés hatására. *Bányászati és Kohászati Lapok, Kohászat*, 3/2016, pp. 9–12.

[9] http://multiserw-morek.pl/products,urzadzenia_do_badania_mas_formierskich_i_rdzeniowych,uniwersalna_maszyna_do_wykonywania_probek_testowych_i_malych_rdzeni_w_technologi_hot-box_cold-box_anorganik_co2 [Accessed May 25, 2021].

[10] Vasková, I., Varga, L., Prass, I., Dargai, V., Coney, M., Hrubovčáková, M. Bartošová, M., Buľko, B., Demeter, P. (2020). Examination of Behavior from Selected Foundry Sands with Alkali Silicate-Based Inorganic Binders. *Metals* 10 (2), 235, February 10, 2020. [Online], Avaible: https://www.mdpi.com/2075-4701/10/2/235/htm. [Accessed May 20, 2021]. http://doi.org/10.3390/met10020235.

[11] Dietert, H. W. (1950). Core knock-out. In: *Foundry Core Practice*. 2nd ed., Chicago, IL: American Foundrymen's Society, pp. 473–478.

[12] Ignaszak, Z. (2018). Discussion on the Methodology and Apparatus for Hot Distortion Studies. *Archives of Foundry Engineering*, Vol. 18, No. 2, pp. 141–145, http://doi.org/10.24425/122517.

[13] Budavári, I., Dargai, V., Varga, L. (2017). Vízüveges maghomokkeverékek melegdeformációs tulajdonságainak vizsgálata „Hot distortion" készülékkel. *Bányászati és Kohászati Lapok, Kohászat*, 5/2017, pp. 15–19.

[14] http://www.simpsongroup.com/model/42114 [Accessed May 25, 2021].

[15] Budavari, I., Varga, L. (2020). The Effect of Coremaking Parameters on the Thermal Distortion Behavior of Resin-Coated Sand. *Material Science and Engineering*, Vol. 45, No. 1, pp. 37–49.

Materials Science and Engineering, Volume 46, No. 1 (2021), pp. 35–42.
http://doi.org/10.32974/mse.2021.004

THE LEACHING BEHAVIOUR OF INDIUM AND IMPURITIES FROM THE LCD GLASS OF SMARTPHONES AND TABLETS

ISTVÁN B. ILLÉS[1] – TAMÁS KÉKESI[2]

Abstract: Primarily, the mechanical removal of LCD panels from smartphones was examined, and a relatively easy and quick manual method was established. The LCD panels can be separated from the rest of the screen in a few seconds. In the cases of more tightly packed applications, the whole screen can be directly ground to a fine powder. The separated LCD screens were leached in different concentrations of HCl and H_2SO_4. The latter was found as practically more advantageous. Leaching with slightly acidic solutions (0.1 M H_2SO_4) results in longer leaching time, however solutions with higher purity can be obtained. If further purification is required, a relatively straightforward method of selective hydrolytic precipitation has also been examined. The practically recoverable amounts of indium may be close to the 400 mg/kg level in a dilute sulphuric acid solution containing less than 10 mg/dm^3 of total impurities (Fe, Zn, Al, Cr, Ni and Cu).

Keywords: LCD, leaching, indium, recovery

INTRODUCTION

Modern flat screen applications rely on indium (In) metal, in the form of a thin coating of indium-tin oxide (ITO). This predominant application represents ~ 90% of the global consumption of this metal [1]. However, there are no individual indium ores, the metal is extracted mainly from the by-products of zinc metallurgy, and to a lesser extent from the refining of tin and lead. Yearly consumption of In is around 1,600 tonnes, with known reserves being only 16,000 tons [2], [3]. Moreover, indium compounds have been found to pose serious health hazards [4], [5]. Thus processing LCD waste has an increasingly strong double incentive. The world produces more than 50 million tonnes of e-waste every year and this value is growing steadily by 3-4% on the yearly bases [6]. It is said that screens, small IT-s, telecommunication devices account for 10% of the aforementioned amounts. In 2020 around 1.38 billion smartphones were sold alone [7]. Hence, this raw material is available abundantly.

[1] Institute of Metallurgy, University of Miskolc
H-3515 Miskolc-Egyetemváros, Hungary
metilles@uni-miskolc.hu
[2] Institute of Metallurgy, University of Miskolc
H-3515 Miskolc-Egyetemváros, Hungary
kekesi@uni-miskolc.hu

1. THE REMOVAL OF THE LCD PANELS

The removal of the indium bearing LCD screen from smart phones (iPhone, Samsung, HTC, and Sony), as well as tablets (iPad, Asus and Samsung) made around the years 2014–2016 were examined with the aim for developing a fast and easy recovery technique. The smartphones have a tightly packed and well-sealed structure, thus the dismantling of the entire phone may prove difficult. The easiest way was found to open up the screen of the devices to pry a screw driver below the top or bottom of the screen and lift up the entire screen package. In most cases, the layers of the screen could be separated easily, and the LCD components could be extracted. However, in the case of more tightly packed screens, the glass layers cannot be separated from each other, requiring a special handling. In this case, the raw material was crushed into a fine powder (<0.5 mm) in a commercial knife mill. Separated LCD panels were deemed good enough to be leached. This separation and preparation process is shown in *Figure 1*.

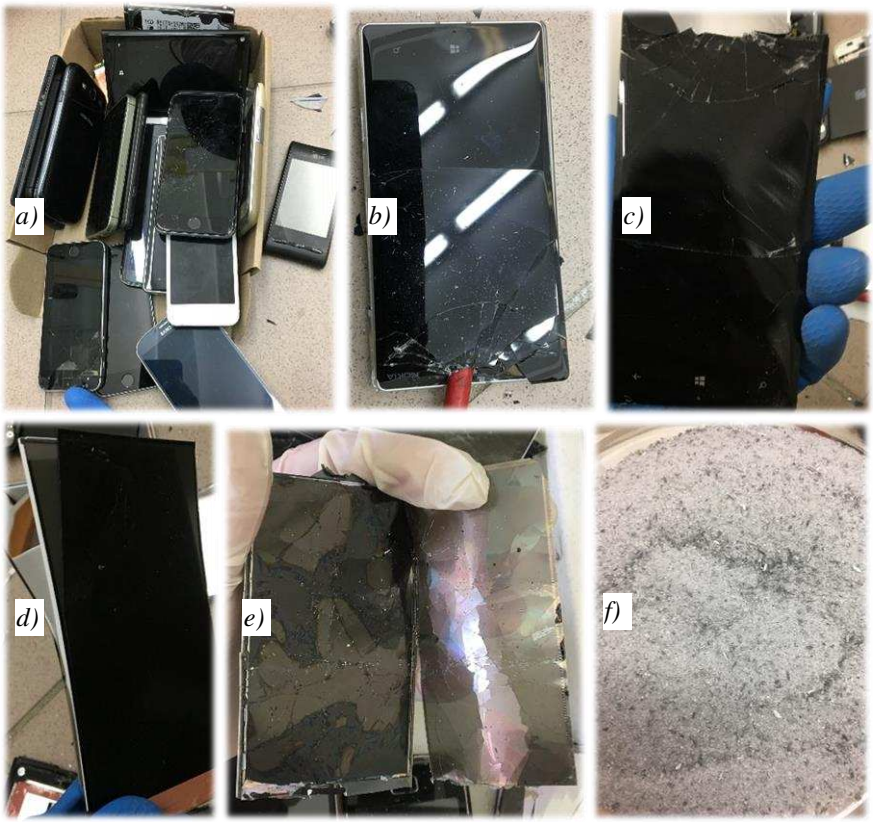

Figure 1

The process for extraction of LCD panels from smartphones: a) – the waste smartphones, b) – prying the screen open, c) – separated screen block, d) – the layers of the screen, e) – separated LCD screens, f) – ground glass powder from the inseparable screen packages

While the procedure requires manual labour, it takes only 30–60 seconds per applications to an untrained lab worker. A similar method was used for the removal of LCD panels from tablets. In this case, the outer glass shielding was simply cracked, and the LCD screens were simply lifted or cut from the frame. It is shown in *Figure 2*.

Figure 2

The removal of LCD panels from tablets: a) – removal of shielding glass, b) – lifting out the LCD screen, c) – separated LCD panels

2. THE EXPLORATORY LEACHING PROCEDURE AND RESULTS

The leaching experiments were carried out in heated conical beakers covered with watch glass lids. After proper dilution of the liquid samples, they were analysed by Atomic Absorption Spectrometry (Varian SpectrAA 300). The hydrolysis experiments were performed in open beakers at room temperature, applying 1 M NaOH neutralizing solution from a burette and stirring at a rate of 150 rpm.

The total leachable metal content of the LCD glass was determined by applying 3 M HCl acid at 90 °C for 2 hours with constant stirring at 350 rpm. The batch consisted of equal amounts of LCD screens extracted from different smartphones and tablets. The liquid/solid ratio was 1 cm^3/g. Results are shown in *Figure 3*.

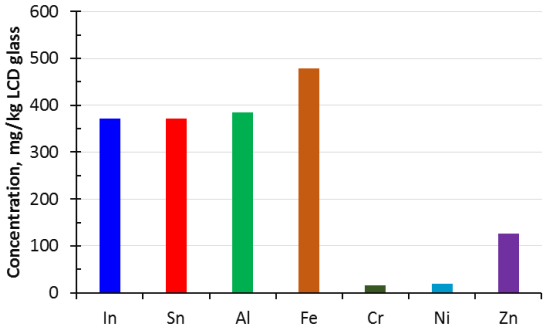

Figure 3

Average leachable metal content of the LCD panels as extracted from the examined smartphones (3 M HCl, 90 °C)

The average leachable indium content was found to be ~372 mg/kg, similar to that of tin and aluminium and iron. The kinetic behaviours associated with the leaching of In and the accompanying (impurity) elements were examined with a smaller batch of the same LCD mix but applying 2 cm^3/g lixiviant ratio at 55 °C. The relative recoveries or the ratios of dissolution – referring to the leachable contents – are shown in *Figure 4*.

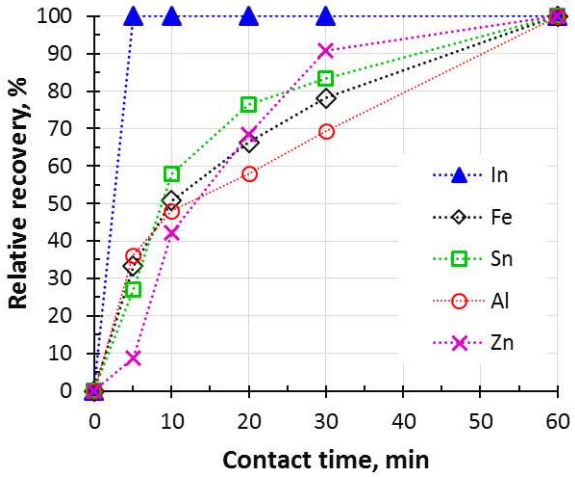

Figure 4

The kinetics of LCD glass leaching (3 M HCl, 55 °C, 350 rpm.)

It can be seen, that 3 M HCl at a mildly increased temperature can solubilize the indium content in 5 minutes, while the major portions of the impurities remain in the solid residue. The composition of the finally obtained solution is shown in *Table 1*.

Table 1

The elemental composition of the leachate obtained with 3 M HCl in 1 h time

	Concentration, mg/dm^3						
In	**Fe**	**Sn**	**Zn**	**Al**	**Cr**	**Ni**	**Cu**
148.4	189.5	27.3	87.5	248.2	12.4	7.6	1.4

Although the leaching rate of indium is quite high, the impurity levels of the solution are also considerable. Thus it may be beneficial to use less acidic solutions to hinder the dissolution of the more refractory accompanying metals, or to include an efficient solution purification step after the intensive leaching. The latter option may be preferred for practical reasons. The known hydrolytic behaviour of the common accompanying elements [8] should be compared to the behaviour of indium. For this reason, we have gradually neutralized a 10 g/dm^3 indium solution while monitoring the pH during the addition of 1 M NaOH solution from a burette under close to equilibrium conditions. The results are shown in *Figure 5*.

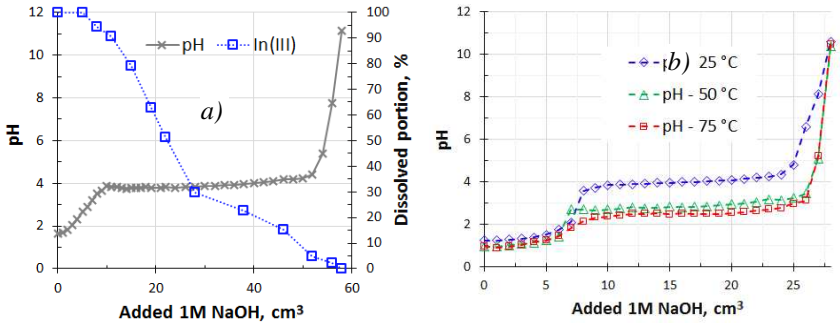

Figure 5

The equilibrium characteristics (a) and temperature dependence (b) of the hydrolytic precipitation of indium

The plateau in the pH curve indicates the metal precipitation by consuming the OH^- ions in the following hydrolysis reaction:

$$In^{3+} + 3OH^- = In(OH)_3 \text{ , } \Delta G°_{298} = 80.5 \text{ kJ/mol } In(OH)_3 \qquad (1)$$

Based on these results, a solution of pH 4 should be able to keep ~10g/dm^3 In in solution at 25 °C. It must be noted also, by increasing the temperature, the pH range of the hydrolysis also decreases and at 75 °C the reaction (1) starts already at not much above pH 2. Most of the base metals (Zn, Cr and Ni) are stable in the solution until the pH reaches significantly higher values than that of indium hydroxide precipitation, therefore they do not interfere with the indium precipitation. Copper is not dissolved from the LCD at any appreciable levels in HCl. Iron and tin can be separated from the solution with relatively good efficiency under reducing conditions at the lower valent states as indicated by the results shown in *Figure 6*.

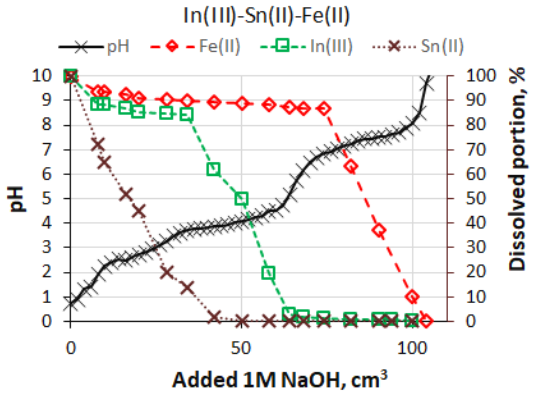

Figure 6

The equilibrium characteristics of the hydrolytic precipitation of In(III), Fe(II) and Sn(II) ions at 25 °C.

However, aluminium, which is an important impurity component according to *Table 1*, has been found to co-precipitate with indium from the leachate. Its separation is impossible by the conventional hydrolytic method. However, if indium is cemented, or cathodically deposited from the solution to obtain a metallic product, aluminium ions can be excluded as potential impurities because of having very negative electrode potential.

3. THE OPTIMIZATION OF LEACHING

Although the method of solution purification may be practically useful, we have tried to decrease the dissolving power of the leaching step. The effect of the pH on the leaching kinetics of In from pure In_2O_3 powder is presented in *Figure 7*.

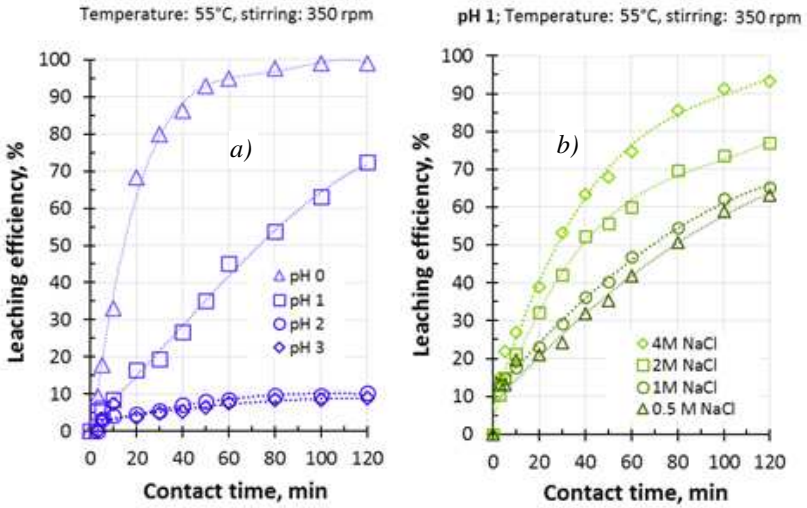

Figure 7
The effect of pH (a) and chloride ion concentration (b) on the leaching rate of indium (L/S = 300 cm³/g)

It can be seen, that leaching at pH 2 and 3 cannot result in recoveries higher than 10%. However, virtually 100% recovery was reached with pH 0 in sulphuric acid (0.5 M H_2SO_4) relatively quickly. Also pH 1 seems to be able to produce satisfactory extraction with longer contact times. The effect of chloride ions was examined at pH 1. Results are shown in *Figure 7.b*. It can be noted, that Cl^- ion concentration in the range of 0.5–1 M did not increase the recoveries. However, in the presence of ~4 M NaCl, the recovery is noticeably higher than in the sulphate solution. It can be attributed to the extra solubilizing effect of the added chloride ions by the formation of chloride complex species.

Further leaching experiments with the LCD glass at milder conditions were conducted using diluted H_2SO_4 and HCl as lixiviants. The raw material was simply cut

into pieces small enough to fit into the neck of the conical beaker. The leaching was conducted at 55 °C with a constant 350 min^{-1} stirring. Results are shown in *Figure 8*.

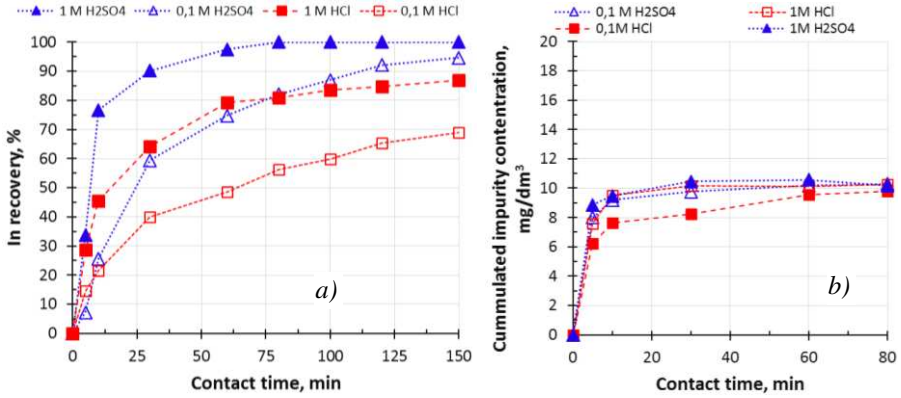

Figure 8

The kinetics curves for the dissolutions of In (a) and of the impurities (b) during the leaching of LCD glass with H_2SO_4 and HCl

The leaching seems to be significantly more effective with the same molarity of sulphuric acid than with HCl as the lixiviant, probably because of the stoichiometrically higher hydrogen ion concentration. The level of impurities in the solution seems to be roughly the same. The composition of the solution obtained by the mild (0.1 M H_2SO_4) leaching is shown in *Table 2*.

Table 2

The composition of the solution obtained by leaching LCD glass with 0.1 M H_2SO_4

	Concentration, mg/dm^3					
In	**Fe**	**Zn**	**Al**	**Cr**	**Ni**	**Cu**
138.9	6.76	1.28	0.43	0.13	0.06	0.01

Comparison of these results to those summarized in *Table 1* shows a definite advantage in terms of solution purity. Indium recovery is still almost complete as suggested by the saturation of the kinetic curve, although at a significantly longer processing time.

CONCLUSIONS

According to the circular economy concept, the smartphone and tablet waste could become a valuable secondary indium raw material. The LCD screens can be removed from the units with a sharp tool by a simple and quick manual operation. In most cases the LCD panels can be easily separated from the rest of the screen. However, more tightly packed screens need to be broken to small particles so as the lixiviant can access the ITO layer. Leaching of LCD panels were examined by HCl and H_2SO_4. The kinetics of the process is definitely improved by higher acid concentra-

tions, but the impurity level is also increased significantly. A relatively simple solution purification by the conventional method of selective hydrolytic precipitation has been shown as practicable. However, the selectivity of the leaching step is advisable to be improved by applying less aggressive reagents. It was found that 0.1M H_2SO_4 was able to leach indium effectively in 120 minutes at 55 °C, with no Sn and relatively little dissolution of other accompanying metals from the initial waste material.

ACKNOWLEDGEMENT

The authors are grateful for Finastra Hungary Co., Ltd. and its Hungarian representative, Mr. Roland Gresnyer, for the valuable cooperation in providing the special electronic raw materials for this research and for its current continuation.

REFERENCES

[1] Li, F., Bai, L., He, W., Li, G., Huang, J. (2015). Resource recovery from waste LCD panel by hydrothermal transformation of polarizer into organic acids. *J. Hazard. Mater.*, Vol. 299, pp. 103–111, http://doi.org/10.1016/j.jhazmat.2015.06.015.

[2] Choi, D., Hong, S. J., Son, Y. (2014). Characteristics of indium tin oxide (ITO) nanoparticles recovered by lift-off method from TFT-LCD panel scrap. *Materials*, Vol. 7, pp. 7662–7669, http://doi.org/10.3390/ma7127662.

[3] Alfantazi, M., Moskalyk, R. R. (2003). Processing of indium: a review. *Minerals Engineering*, Vol. 16, pp. 687–694, http://doi.org/10.1016/S0892-6875(03)00168-7.

[4] Chou, W. L., Huang, Y. H. (2009). Electrochemical removal of indium ions from aqueous solution using iron electrodes. *J. Hazardous Mater.*, Vol. 172, pp. 46–53, http://doi.org/10.1016/j.jhazmat.2009.06.119.

[5] Lim, S. R., Schoenung, J. M. (2010). Human health and ecological toxicity potentials due to heavy metal content in waste electronic devices with flat panel displays. *J. Hazardous Mater.*, Vol. 177, pp. 251–259, http://doi.org/10.1016/j.jhazmat.2009.12.025

[6] Illés B., Nagy S., Kékesi T. (2020). LCD-hulladékból történő indium fémkinyerés hidrometallurgiai úton. *BKL-Kohászat*, Vol. 153, No. 5–6, pp. 22–31.

Materials Science and Engineering, Volume 46, No. 1 (2021), pp. 43–53.
http://doi.org/10.32974/mse.2021.005

THE POSSIBILITY OF RARE METAL RECOVERY FROM WHITE LED BULBS

ISTVÁN B. ILLÉS[1] – SÁNDOR NAGY[2] – TAMÁS KÉKESI[3]

Abstract: White LED bulbs – dominant in lighting technology – can become a significant secondary source for the recovery of valuable rare metals, if a proper extractive metallurgical technology is developed. We have found an efficient way to separate the "phosphors" (phosphor coated LED chips) from the metallic base shells in dilute sodium carbonate and calcium hydroxide solutions. The leaching reactions of the separated phosphors was studied thermodynamically and the process was examined experimentally. The contained base metals and rare earth elements could be efficiently leached in 1 M HCl acid in 1 h, only Ga and In showed inert behavior toward acid solubilization. The separation of the valuable components has been devised by standard hydrometallurgical techniques.

Keywords: LED lighting, recycling rare earth metals, recovery

INTRODUCTION

The electric lighting is indirectly responsible for ~5% of the total CO_2 emission. [1] Thus the traditional – not energy efficient – tungsten-based incandescent light bulbs are being phased out all over the world. In some countries their marketing is completely prohibited. [2] On the other hand, the application of light emitting diode (LED) technology is increasing rapidly. These light bulbs offer much longer lifetime, significantly reduced energy consumption while producing the same amount of light as the incandescent bulbs. [2] Moreover, the energy loss in the form of infrared light is also negligible in the case of LEDs. Based on estimations, approximately 95% of the lighting market will be dominated by LED light sources by 2025. [3]

However, LED light bulbs require some critical raw materials, such as rare-earths, indium and gallium. The most common white light producing LED technology applies an indium-gallium-nitride semiconductor chip on a sapphire substrate, which directly emits blue light in the 440–470 nm range. The chip is enveloped in a

[1] Institute of Metallurgy, University of Miskolc
H-3515 Miskolc-Egyetemváros, Hungary
metilles@uni-miskolc.hu
[2] Institute of Raw Materials Preparation and Environmental Processing, University of Miskolc
H-3515 Miskolc-Egyetemváros, Hungary
ejtnagys@uni-miskolc.hu
[3] Institute of Metallurgy, University of Miskolc
H-3515 Miskolc-Egyetemváros, Hungary
kekesi@uni-miskolc.hu

material called phosphor that converts this primary radiation into a warmer tone, which the human eye perceives as white light. The phosphor used for this technique is most often yttrium aluminium garnet doped with cerium, $Y_3Al_5O_{12}:Ce^{3+}$ (YAG:Ce). Other versions such as $(Y,Gd)_3Al_5O_{12}:Ce^{3+}$, (YGAG:Ce), $(Y,Tb)_3Al_5O_{12}:Ce^{3+}$ (YTAG:Ce), $Y_3(Al,Ga)_5O_{12}:Ce^{3+}$, (YAGG:Ce), $Y_3Al_5O_{12}:Ce^{3+},Pr^{3+}$, (YAG:Ce,Pr), $Lu_3Al_5O_{12}:Ce^{3+}$ (LAG:Ce) and BOSE $(Ca,Sr,Ba)_2SiO_4:Eu^{2+}$ and CASN $(CaAlSiN_3:Eu^{2+})$ are applied also in LEDs. [4], [5], [6] A light source of 1 mm^2 surface area with two LED chips contains ~3 μg Ce or Eu, while elements like Y, Lu, or Gd – which form the basic matrix of the phosphor – are present in higher amounts (approx. 90–200 μg). Moreover ~17–30 μg Ga and In can be found in such a chip. Noble metals like Au (~200 μg) – used as current conductor filaments – can also be found in the LEDs. [7] The recycling of LED waste is not yet practiced, mainly because of the implied novelty. However, the LED industry is expanding rapidly, thus a large supply of these waste materials can be expected in the near future.

1. CHARACTERIZATION AND PREPARATION OF THE RAW MATERIAL

The aim of this work was to examine LED waste materials – gathered from residential applications – in order to assess their metal value and gain fundamental data which can aid the development of a recycling method. The complex structure of a LED bulb makes its recycling difficult, thus before a metallurgical procedure can be developed, their general structure and composition must be explored. The examined LED bulbs of different structural designs and the mechanically removed LED units – including the attached motherboard strips or plates - are shown in *Figure 1*. In the case of the bulb in *Figure 1a*, the electric components are originally attached to the motherboard, however they were removed before the LED unit was taken to the processing steps.

Figure 1
The examined LED bulbs (a–c) and the removed LED units (d)

Unlike incandescent bulbs, LEDs use printed circuit boards, two or more capacitors and coils, which further increase their value as these components can contain Cu, Sn and Ta in not negligible quantities. The mechanically detached LED units containing

the light emitting seeds were examined under the microscope, as shown in *Figure 2*. In general, the LED units consist of the yellow phosphor seed, the LED chip *(Figure 2c)*, the metallic container tray *(Figure 2b)*, the motherboard strip or plate *(Figure 1d)* and the soldering butts at the terminals of the metallic trays *(Figure 1a, b)*. These LED units constitute the principal parts which generate the light upon receiving the proper voltage. The surface of the aluminium- or plastic-based multi-layered motherboard is covered with a non-conductive organic sealing or paint, underneath there are current conductor layers made of isolated copper foils. The container trays of the LED units are attached to these conducting layers.

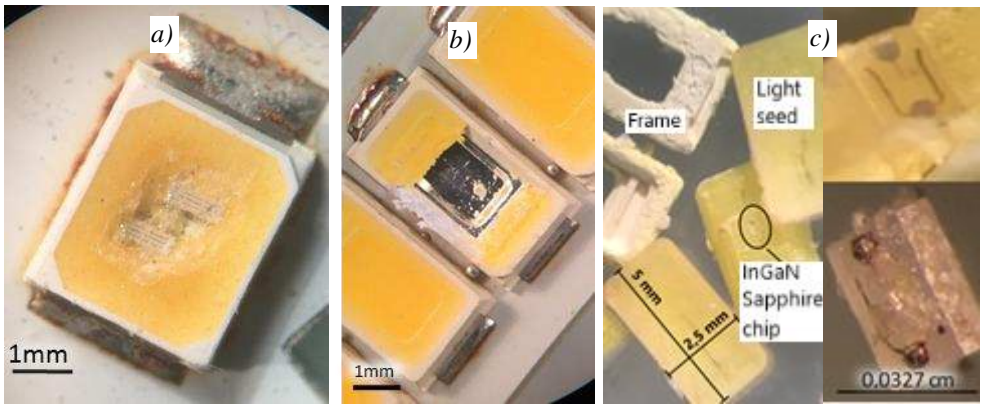

Figure 2

Two LED units removed from the motherboard strips (a, b), separated phosphors (c) and the LED chip physically separated from the phosphor coating (d)

The LED chip is laid on a metallic tray – confirmed to be of silver plated steel – and enveloped in the phosphor, which is fixed in a plastic/ceramic frame. The current is conducted from the terminals of the LED unit to the chip through the phosphor via a gold filament. One such LED unit can contain one or multiple LED chips.

Each different type of the collected LED bulbs was dismantled and the major components determined. Results are shown in *Table 1*. The bulbs contain large amounts of plastic/ceramic or glass components, requiring a complex treatment.

Table 1

The distribution of the individual components of the LED bulbs in mass-%

Type	LED units	E. circuit	Steel base	Glass	Plastic/ceramic
Figure 1*a*)	8.97	7.48	3.17	–	80.4
Figure 1*b*)	32.33	5.11	3.41	–	59.13
Figure 1*c*)	13.12	6.59	1.23	64.08	14.6

We have examined the total metal content of the LED units – as attached to the motherboard pieces – by leaching in 12 M HCl, 15 M HNO_3 and aqua regia, respectively at boiling temperatures. The solutions were analysed by microwave plasma emission spectroscopy (MPOES). The highest extracted amounts by any of the lixiviant media were accepted as the representative metal contents. The base metal content of the LED units, as dissolved by aqua regia at boiling temperature, can be seen in *Figure 3*.

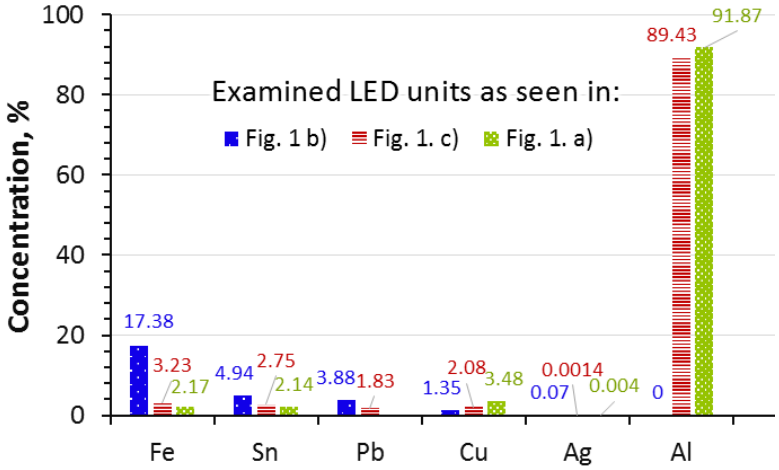

Figure 3

Dissolved base metal content of the examined LED units (aqua regia: 10 cm^3/g)

Aside from Al – which is the motherboard material of the LED units in more durable LED bulbs – the concentrations of Fe, Sn, Pb and Cu are also significant. The prices of these metals strongly depend on their respective purity. Thus Sn and Cu recovery could contribute to the economic incentive for recycling. Moreover, the removal of heavy metals such as Pb could also be beneficial for environmental protection. While iron carries relatively little value neither is toxic, a complex recycling technology could provide some valuable iron compounds too.

The valuable rare metals are contained in the usually yellow colored phosphor seeds fixed in the metallic container trays and thus attached by soldering to the motherboard. The complete dissolution of the solder butts and the partial dissolution of the Ag layer on the metallic container trays result in the separation of the phosphor seeds with the LED chip remaining enclosed. The liberated phosphor seeds (of less than 2.5 mm diameter) were separated from the large pieces of the mixed residue by sieving and were subjected to crushing and grinding in a mortar. The obtained powder was than leached in aqua regia at boiling temperatures. The rare earth content could be accessed partly also directly by the preliminary leaching of the LED units. The remaining part was leached subsequently from the separated phosphor seeds after fine grinding. The results obtained by the consecutive leaching steps are presented in *Figure 4*.

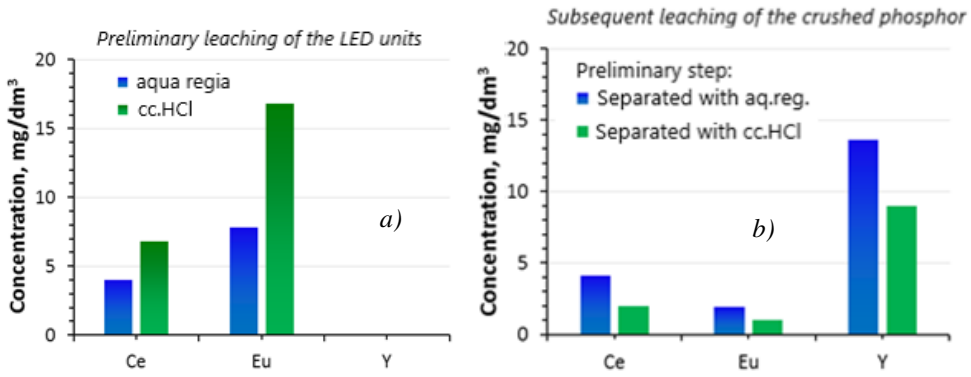

Figure 4

Relative amounts of rare metals dissolved directly from the LED units (a) and from the separated and crushed phosphor with aqua regia (b.) (20 g LED units, or 1.84 g phosphor seeds removed, 40 cm³ solution, 350 rpm, 2 h boiling)

As shown by the comparison of *Figures 4a* and *4b*, most of Ce and Eu has dissolved from the phosphor during the preliminary liberating step applying strong acids. However, all the Y remained to be dissolved in the subsequent leaching of the separated and crushed phosphor seeds. The $Y_3Al_5O_{12}$ is composed of two oxides with high thermodynamic stability, thus it is hard to dissolve. On the other hand, the solution from the first leaching step infiltrated the phosphor, thus some of the Ce and Eu may have been carried over physically entrapped in the phosphor to the subsequent leaching step. This mechanism explains why the impurity levels shown in *Figure 5* were found relatively high in the leachate of the crushed phosphor.

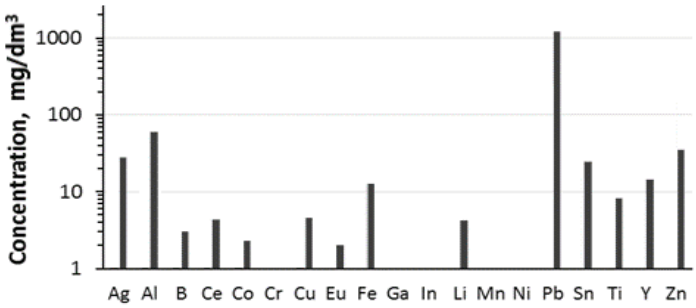

Figure 5

The metal concentration of the aqua regia solution obtained from the leaching of the phosphors previously separated from The LED units with cc. HCl (1.84 g phosphor seeds, 40 cm³ solution, 350 rpm, 2 h boiling)

After leaching, the solution was cooled and the poorly soluble Pb salts crystallized inside the phosphor. Moreover, during leaching the solution quickly becomes saturated in $PbCl_2$, thus the crystallization can occur even during the leaching. The com-

plex composition and the high impurity content would make the economically feasible rare metal recovery difficult. Thus to selectively solubilize the rare metals, the phosphor and LED chip must be preliminarily separated from the panel and the base of the LED unit, while avoiding the dissolution of the base and rare metal content.

2. SEPARATION AND PREPARATION OF THE PHOSPHOR SEEDS

The valuable rare earth metals are concentrated in the phosphor seeds contained in the LED units. A selective removal of the phosphor layer – including the LED chip – from the LED unit and the attached motherboard can be achieved by boiling the units in a mildly alkaline medium. The examined agents were Na_2CO_3, $Ca(OH)_2$, and water. The best results were obtained with saturated $Ca(OH)_2$ solutions, but with a longer time, the dilute Na_2CO_3 solution was also efficient. Results are shown in *Figure 6*.

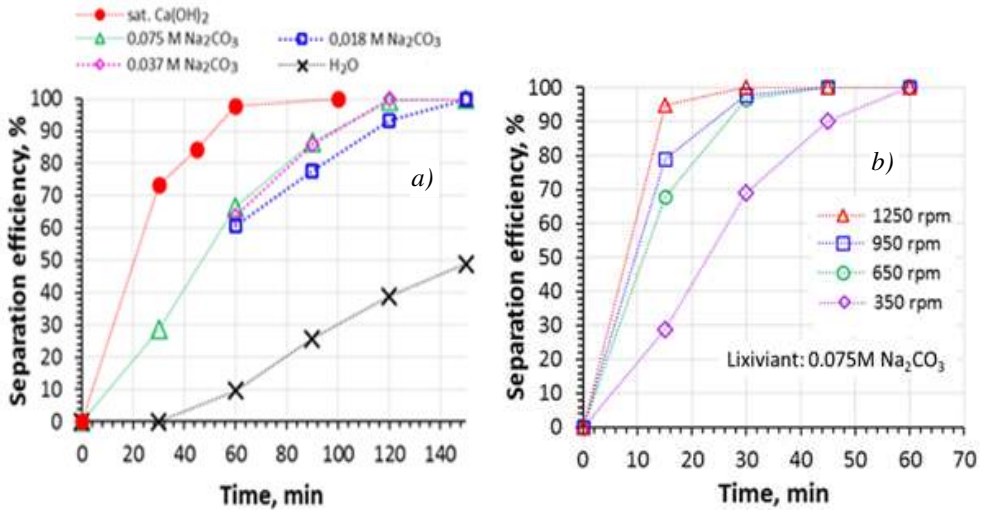

Figure 6
Separation efficiencies of the phosphor seeds in different media (a); the effect of stirring speed on the separation efficiency (b)

Applying pure water assures only rather low separation efficiencies. In contrast, saturated $Ca(OH)_2$ solutions seems to be the most effective at separating the phosphor, followed by the dilute Na_2CO_3. It must be noted that this separation process has been only tested on used LEDs. Thermal aging processes during usage weakens the structure and bonding between the phosphor and its surroundings. The LED motherboard pieces and the phosphors were separated from each other by sieving. The latter was ground into a fine powder with a ceramic mortar and a pestle. The separation process and the products are shown in *Figure 7*.

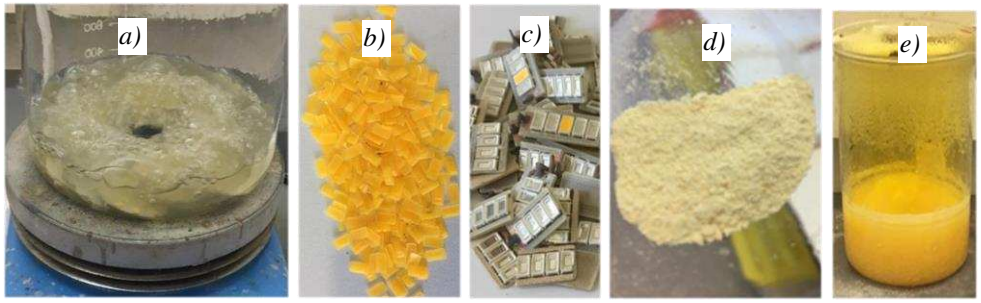

Figure 7

The separation of the phosphor including the LED chip in an alkaline medium (a); the separated phosphor seeds (b); the residue bearing base metals (c); crushing the phosphor (d); leaching of the phosphor powder (e)

3. RARE METAL DISSOLUTION FROM THE PHOSPHOR SEEDS

The viability of leaching the phosphor has also been examined thermodynamically. The most valuable components are the phosphor matrix itself ($Y_3Al_5O_{12}$) doped with Eu and Ce and the semi-conductor (InGaN) layer on the LED chip. Calculations were carried out using the HSC Chemistry software. The considered aqueous reagents were H_2SO_4, HCl and HNO_3. The standard Gibbs free energy change of the aqueous reactions are plotted as functions of the temperature in *Figure 8.*

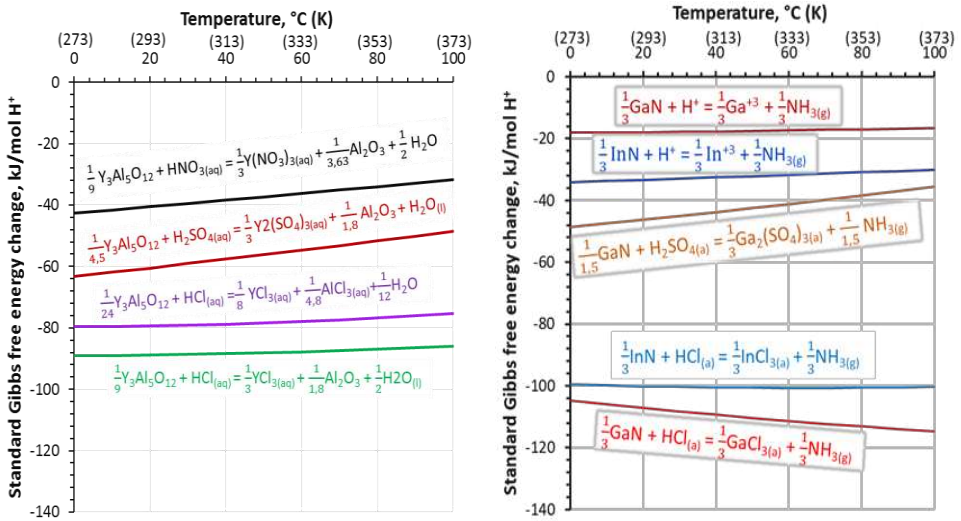

Figure 8

The temperature dependence of the standard Gibbs free energy change accompanying the leaching of the YAG compound (a) and the semiconducting LED material (b) with different solvents

It can be seen, that HCl acid has superior solubilizing power compared to cheaper sulphuric and the strongly oxidizing nitric acid. The relatively largely negative standard Gibbs free energy change of the reactions in aqueous media suggests, that the dissolution of the metals in the InGaN semiconductor chip is feasible. However, the nitrides are known to behave as refractory toward leaching in virtually any kind of aqueous solvents. It could be only effected at elevated pressures and temperatures, or after a thermal conversion via alkaline roasting. [8]. This has been confirmed by our results of the experimental digestion *(Figure 5)* aimed at the complete dissolution of the LED units. This inert nature could be advantages, as the other more soluble components (such as rare earth metals and most impurities) can be dissolved, while the Ga and In remain in the solid residue, thus selective retention can be achieved. It is convenient that the aqueous ions of the rare earth metals can be kept stable at relatively high pH values. *Figure 9* shows the E-pH diagrams of Eu, Ce and Y.

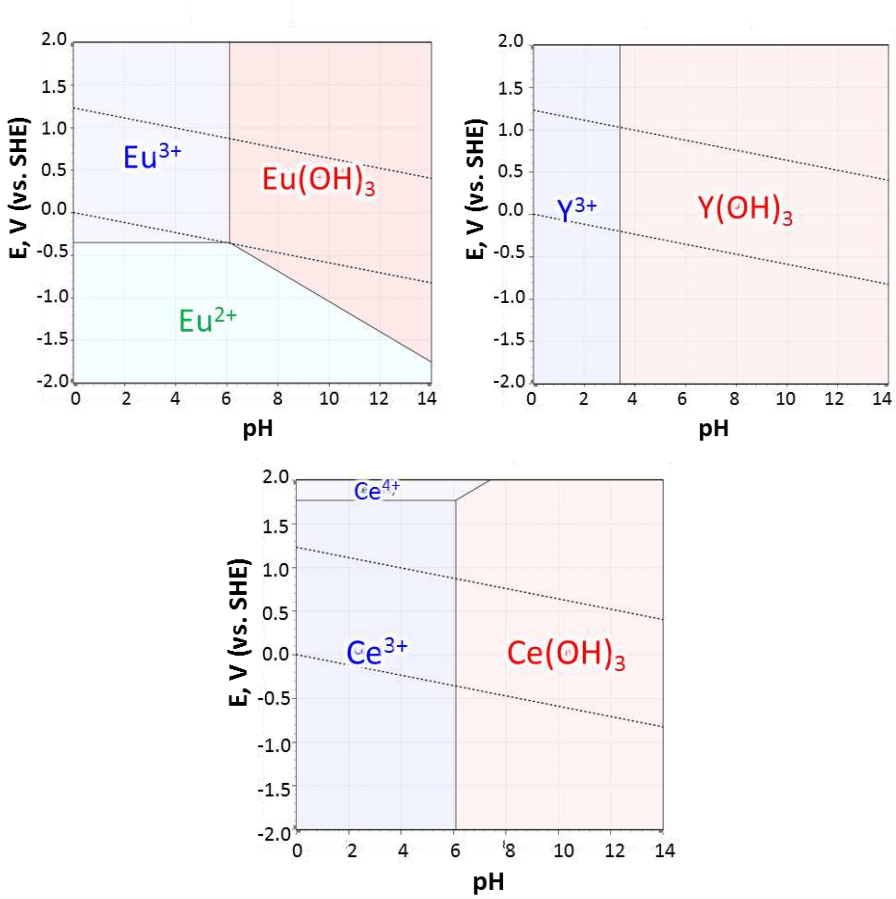

Figure 9
The E-pH diagrams of Eu, Ce, Y (25 °C, dissolved metal: 1 mol/dm³)

One of the main challenges in extracting pure rare earth metals is their very similar chemical behaviour. While Y is not one of the lanthanides, still it is chemically similar to this group. The Pourbaix-diagrams suggest that the hydrolysis of Y can be expected at lower pH. However, the activity conditions may alter the predominance limits of the indicated ions. Based on the published stability constants of the respective hydroxides, [9] we have calculated and plotted the pH dependence of the equilibrium Ce^{3+}, Eu^{3+};Y^{3+} ion concentration. This is presented in *Figure 10*.

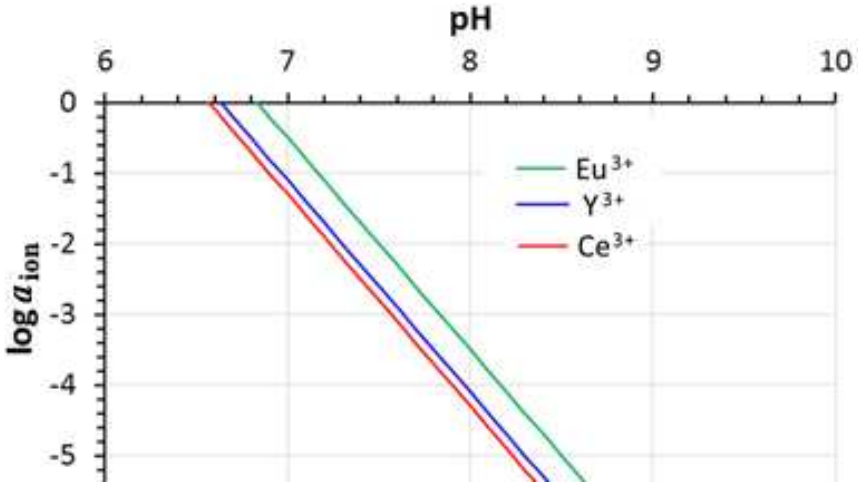

Figure 10

The equilibrium activities of dissolved rare earth metal ions as functions of the pH

Based on the equilibrium curves, the hydrolysis of the phosphor components can only be expected above pH 6. Thus close to neutral conditions could be applied at the end of the leaching step. This would significantly reduce the Fe(III) and Al concentration in the leachate.

The separation of the phosphor seeds in alkaline media results in low impurity levels in further steps of rare earth recovery, as practically no reaction took place during the preliminary leaching. Besides the rare earth metals, the recovery of noble metals (Au, Ag) could also become important, as Au constitutes ~0,6% and Ag ~0,2% of the total weight of the phosphor. It would be beneficial if the rare metals and other impurities could be dissolved from the residue without the dissolution of the noble metals. As the thermodynamic study suggest, HCl can be a suitable solvent. Therefore, further leaching experiments were carried out at 60 °C using 1 M HCl with 350 1/min stirring speed. The relative recovery rates are plotted in Fig. 11 as compared to the values obtained by a virtually complete digestion with aqua regia at boiling temperatures for 3 hours. Dopant materials (Eu, Ce) can be dissolved from the YAG matrix much faster than Y, which is possibly due to the higher stability of the YAG double oxide. Thus if Y dissolution is desired, longer time and higher temperatures are required.

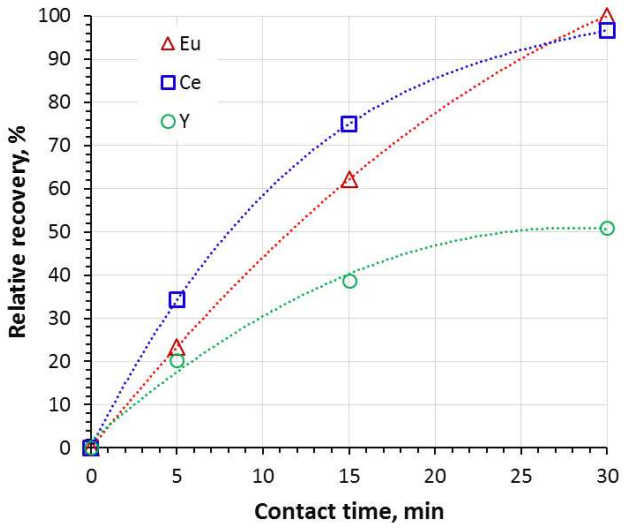

Figure 11

Relative recoveries of the rare earth metals from the phosphor powder by leaching with 1 M HCl at 60 °C, as compared to the total metal content determined by aqua regia leaching at boiling temperature

CONCLUSIONS

The end-life white LEDs were examined physically, it was found that the LED motherboard and panel contains significant amounts of metallic aluminium and copper, while further values (Pb, Sn) can be found in the solder. The LED units hold the phosphor and the LED chip itself, which contains rare earth metals along with Ga and In. The physical separation of the phosphor – including the LED chip – was best achieved via slightly alkaline treatment. The fastest separation was achieved with a saturated $Ca(OH)_2$ solution, while 0,075M Na_2CO_3 could produce similar results at longer times. The solubilisation of the separated phosphor and LED chip was first studied thermodynamically, proving that HCl has superior solubilizing power when compared to H_2SO_4 and HNO_3. The stability diagrams showed that neutral leaching could be considered also for a cleaner extraction of the rare metal oxides. Experimental leaching proved, that the rare metals can be leached efficiently from the separated and crushed phosphor seeds in 1 M HCl at 60 °C. If Au is also to be recovered, aqua regia leaching at boiling temperature may be applied.

ACKNOWLEDGEMENTS

The research was carried out at the University of Miskolc both as part of the project (TUDFO//51757/2019/ITM) implemented in the framework of the Thematic Excellence Program funded by the Ministry of Innovation and Technology of Hungary, and the project supported by the Ministry of Innovation and Technology of Hungary from the National Research, Development and Innovation Fund in line with the

Grant Contract issued by the National Research, Development and Innovation Office. The authors are grateful to dr. Márton Tóth for executing the complex task of analyzing the exploratory solution samples by the MPAES technique.

REFERENCES

[1] Kitai, A. (2011). *Principles of solar cells, LEDs and diodes. The role of the PN junction*. Mississauga: Wiley.

[2] Held, G. (2009). *Introduction to Light Emitting Diode technology and applications*. Boca Raton: CRC Press.

[3] McKittrick, J. (2013 Oct.). *Solid State Lighting Program: Final Report*. [Online]. Available: https://www.osti.gov/servlets/purl/1113955.

[4] Inamuddin, K. Anish, Abdullah, A. M. (2020). *E-waste Recycling and Management*. Cham, Switzerland: Springer.

[5] Chen, W.-S., Hsu, L.-L., Wang, L.-P. (2018). Recycling the GaN waste from LED industry by pressurized leaching method. *Journal of Metals*, Vol. 8, No. 10, Article number: 861, http://doi.org/10.3390/met8100861.

[6] Sillén, L. G., Martel, A. E., Bjerrum, J. (1964). *Stability constants of metal-ion complexes*. London: Chemical Society.

Materials Science and Engineering, Volume 46, No. 1 (2021), pp. 54–62.
*https://doi.org/*10.32974/mse.2021.006

THE EFFECT OF FEEDING OF RAW MATERIAL ON GAS CHARACTERISTICS DURING THERMAL DECOMPOSITION

GÁBOR NAGY[1]

Abstract: Pyrolysis and gasification are thermochemical processes that have gained significant attention in the past decades. During pyrolysis, numerous parameters can affect the final solid, liquid and gaseous products. The pyrolysis of oak wood samples at 700 °C with three different feeding times were carried out under laboratory conditions. The gas yield was the highest with the use of the lowest feeding speed (11.5 min residence time), resulting in over 20% increase in the quantity of produced gas. Faster feeding speed results in shorter residence time in the heated zone, hindering the degradation of hydrocarbon. The LHV recorded at all experiments are applicable for energy purposes. On the other hand, due to the low H_2/CO ratios (<1), none of the experiments produced syngas usable for the chemical industry.

Keywords: pyrolysis, feed rate, syngas

INTRODUCTION

The thermochemical utilisation of solid fuels dates back as far as human history. However, during the past decades, the main focus has shifted toward the use of thermochemical processes resulting in fuels with different physical states or value-added products.

Thermochemical processes include pyrolysis (thermal decomposition) and gasification. During pyrolysis, the base material is heated to 400–1000 °C temperature interval under anaerobic or anoxic conditions to carry out the thermal decomposition of the material. As a result, liquid and gaseous products are produced along with solid char, which could mainly be used for energy purposes. In case of gasification, the aim is to produce a high quantity of gaseous products from solid base materials using partial oxidation at high temperature (over 800 °C). The gas can be used as fuel of base material for the chemical industry.

The changes in the ratios and qualities of the products are regulated by numerous parameters. For both processes, temperature and residence time are significant. Higher temperature and longer residence time have a positive effect on raw material conversion: if the residence time is longer, light molecular weight hydrocarbons, non-condensable petroleum gases are produced which have considerable thermal stability [1].

[1] Institute of Energy and Quality, University of Miskolc
H-3515 Miskolc-Egyetemváros, Hungary
nagy.gabi@uni-miskolc.hu

Residence time can only be regulated in continuous operation system by the changing the feeding speed of the base material, for example by increasing the rotational speed of the screw in a screw reactor the base material can be passed through the system faster. In case of batch operation, residence time refers to time interval from the beginning of heating the raw material to the time when the products are removed from the system.

Increasing the temperature can accelerate thermal decomposition, so the modification of two parameters can be used to optimise the energy consumption of the system and increase the yield of the main product.

As pyrolysis can be used independently or as a part of a gasification system, the main focus of the literature overview and the experiments was pyrolysis.

Numerous studies experimented with the effects of using different feeding systems. Singh et al. [2] examined the effect of residence time (1, 2 and 3 hours) for the pyrolysis of mustard straw at 250–500 °C in a fixed bed reactor. Based on their results, pyrolysis temperature had a more significant impact than the increased retention time for this particular raw material. Ningbo et al. [3] carried out pine sawdust pyrolysis in a screw reactor at 600 °C using 3, 4, 5, 6 and 7 minutes of retention time. It was concluded that increasing retention time reduced the quantity but increase the calorific value of the solid residue. Moreover, in case of the syngas, the longer residence time resulted in lower content of CO_2 and higher content of CO, H_2 and C_1-C_4 hydrocarbons. Ha et al. [4] carried out fast pyrolysis experiments in bubbling fluidized bed reactor at 426–528 °C temperature range using 0.8-1.8 kg/h feeding rate. The base material was wood sawdust. The increase of feeding rate from 0.8 to 1.8 kg/h during fast pyrolysis had marginal influence in the quantity of the products. Hsu et al. [5] also used fluidized bed reactor for pyrolysis of rice husk at 600 °C reactor temperature, with 10 and 20 g/min feeding rate. As a result of their experiments, it was concluded that not only the feeding speed impacted the quantity of the products, but the carrier gas flow rate, as well. With lower flow rate (30 l/min), the higher feeding rate increased the char quantity and decreased the gas yield. However, the higher flow rate (40 l/min) and increased feeding rate resulted in lower char and higher gas quantity. The reason for this was that higher carrier gas flow rate can enhance the contacts between the base material and the fluidizing glass beads. Newalkar et al. [6] pyrolyzed Loblolly pine in an entrained flow reactor at 600–1,000 °C temperature range and 5–20 bar pressure with 4 and 28 s residence time. It was concluded that longer residence time for the base material increased the residual carbon and decreases the H/C and O/C ratios of the char, especially at higher temperature (1,000 °C). The increase in temperature, pressure, and residence time decreased the concentration of C_2–C_4 hydrocarbons in the gas.

Based on the relevant literature, the effect of feeding speed can vary for each measurement. The quantity and quality of products can change because of the type and operational parameters of the equipment. Thus, the operational parameters should be modelled under laboratory conditions, first.

One of the aims of my experiments was to prepare a laboratory system applicable for pyrolysis and gasification in which batch and continuous operation. Furthermore,

experiments with different feeding speeds were carried out in the system using biomass base material, examining the possible utilisation of the produced gas.

1. MATERIALS AND METHODS

1.1. Materials and methods

Oak wood naturally dried for one year was used as a base material for the experiments, whose properties are summarized in *Table 1*.

Table 1

The properties of the base material

Average composition of the dry samples, %w/w						**Original base material, %w/w**
Carbon	Hydrogen	Nitrogen	Sulphur	Oxygen	Ash	Moisture
47.79	6.19	0.11	0.01	39.98	5.92	9.26

The standard used for the elemental composition of the samples carried out with a Carlo Erba EA 1108 elemental analyser was *"EN 15104-2011: Solid Biofuels – Determination of Total Content of Carbon, Hydrogen and Nitrogen – Instrumental Methods"*. To determine the ash content, standard *"EN 14775:2010: Solid Biofuels – Determination of Ash Content"* was used, the measurement was carried out in a HK-45/12 V type heating furnace with 12 kW nominal power. The moisture content was determined using a Mettler Toledo HB43-S type moisture analyser.

Two Medingen type rotameters (3–30 and 20–260 l/h) were applied to examine the quantity of the produced gas. To be able to compare the l/h values of gas products from the different amounts of base materials, they were converted to l/1 kg base material.

The gas composition was determined with a Dani Master GC device, equipped with a TCD detector and an S/SL injector. 3 columns were connected in series for the separation of gas components: Rt-Q-bond (15 m × 0.53 mm × 20 μm), Rt-Q-bond (30 m × 0.32 mm × 10 μm) and Rt-Msieve 5A (30 m × 0.53 mm × 50 μm).

The lower heating value (LHV) of the gas mixtures was calculated using the LHVs of each component found in literature (*Table 2* [7]) using the measured concentrations.

Table 2

LHVs of gas components [7]

Components	LHV, MJ/m^3
Methane	35.949
Ethane	64.615
Ethylene	59.571
Carbon monoxide	12.680
Hydrogen	10.826

1.2. Experimental system

The experiments were carried out in a laboratory system applicable for pyrolysis and gasification *(Figure 1/a)*. Both batch *(Figure 1/a)* and continuous *(Figure 1/b)* operation can be modelled under laboratory circumstances. In the article, the pyrolysis was carried out at 700 °C. After filling the reactor inside the tube furnace, heating was performed for 30 min, then the reactor temperature was kept constant at 700 °C until the end of the experiment. Continuous operation was achieved with filling the whole reactor that was 3× longer than the tube furnace with base material, and the heated zone of the furnace was moved along the reactor at given time intervals. The displacement of the heated zone was executed after the gas production decreased below 0.5 l/kg during the holding time. With the used amount of material, the feeding time was 10 minutes. Furthermore, the experiments were carried out with 15% faster and slower feeding time (8.5 and 11.5 minutes of feeding time).

During the detailed experiments, 70±3 g material was uniformly distributed in the pipe reactor. The amount of material in the heated zone is 25–30 g, while the rest is in the remaining part of the pipe, so it could be fed through the reactor in seven steps (6-7 g raw material for each step).

As it can be seen in *Figure 1/a*, the gas and liquid discharged from the reactor are collected in a liquid container with a gas cooler on the top, so the condensed liquid could also accumulate in the container. After the cooler, a rotameter is placed, and the gas can be sampled before it reaches the torch. The system can be expanded with a vapour generator to prepare a system applicable for continuous gasification.

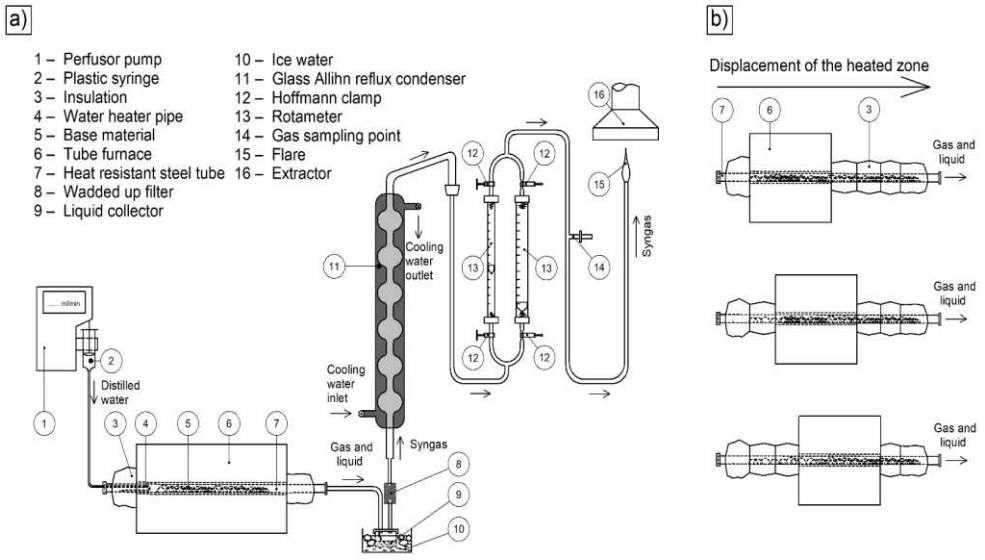

Figure 1
The experimental system for pyrolysis and gasification (a), and the feeding process (b)

2. RESULTS

The gas production, recorded minute-by-minute, was converted to 1/kg and the results are illustrated in *Figure 2*. As it can be seen in the figure, the gas production of the 700 °C pyrolysis started to decrease after 30 minutes. By the 38th minute, the gas production was below 0.5 l/h according to the rotameter, then the feeding of the base material started (with the displacement of the heated zone). In case of all three tests, the first feeding step resulted in significantly higher gas production compared to the later steps, as the time to pre-heat the base material was longer before the first displacement could start. The examination of the total feeding reveals that the increased feeding speed resulted in steadier gas production. However, this entails the decrease of the total amount of produced gas. The produced gas quantities can be seen in *Table 3*.

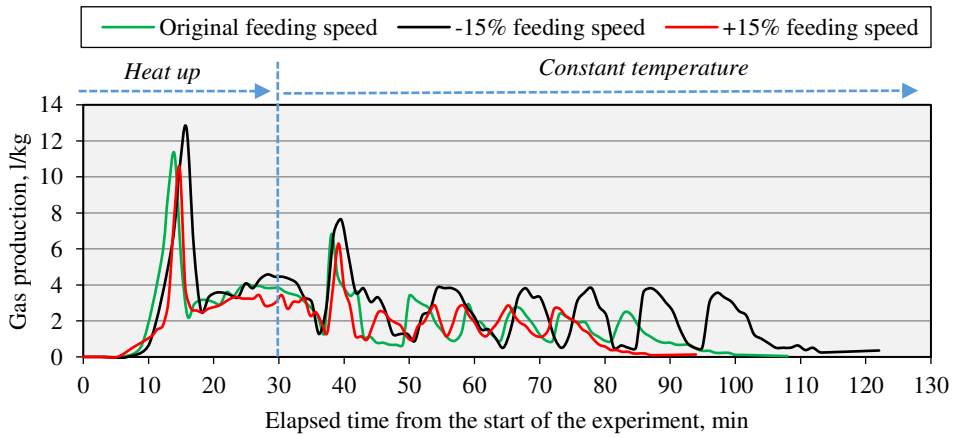

Figure 2
The effect of feeding on gas production

Table 3
The amounts of produced gas during the experiments

Experiment	–15% feeding speed	Original feeding speed	+15% feeding speed
Gas production, l/kg	253.5	207.3	200.3

The changes in the produced gas composition are illustrated in Figure 3. All three experimental series started with a 700 °C pyrolysis starting from room temperature, then the tests with different feeding speeds were carried out. The formation of hydrocarbons started with the temperature increase during pyrolysis. The hydrocarbons expelled the air from the reactor and CO and CO_2 was produced via combustion. With the depletion of oxygen, the amount of CO and CO_2 decreased and the release

of oxygen from the base materials led to the increase in CO content. Parallelly, the amount of hydrogen increased, and the hydrocarbon content decreased until a relatively constant value was reached. During the first feeding step, there was no considerable change in the quantity of the components, as the pyrolysis of the base material could start through the prolonged holding time. However, the subsequent feeding steps had more significant effect on the gas composition. Considering the generation of the most important components for syngas utilisation (H_2, CO and C_xH_y), the lowest feeding speed resulted in the steadiest production. Increasing the feeding speed, the hydrocarbon production remained steady, while the other components (H_2, CO and CO_2) showed considerable fluctuation. According to the gas composition analysis, the reduced feeding speed leads to a steadier gas composition over the duration of pyrolysis.

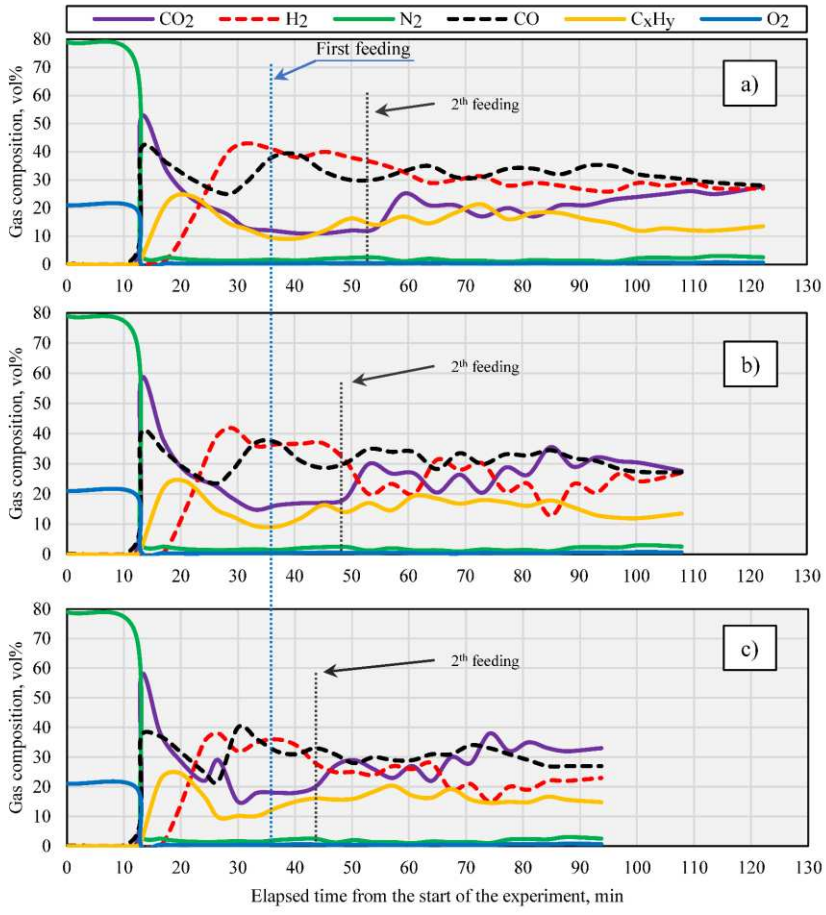

Figure 3

The changes in gas composition with –15% (a), the original (b) and +15% (c) feeding speed

Based on the average composition of the produced gases *(Table 4)*, increased feeding speed resulted in lower H_2 (–7%) and CO (–2%), but higher C_xH_y content (+3%). If the feeding is faster, the base material has shorter residence time in the heated zone Thus, the rate of pyrolysis is lowered and there is no time for the further degradation of hydrocarbons.

Table 4

The average composition of the produced gases

Parameter	**–15% feeding speed**	**Original feeding speed**	**+15% feeding speed**
H_2	26.7	23.3	21.8
CO	30.2	29.2	28.6
C_xH_y	13.6	13.8	14.2

For energy purposes, the Lower Heating Value (LHV) of the gas is significant, while the hydrogen-to-carbon monoxide ratio can determine the possible use in the chemical industry. The changes of these values in relation to time are shown in *Figure 4*, and the average values during the experiments are summarised in *Table 5*.

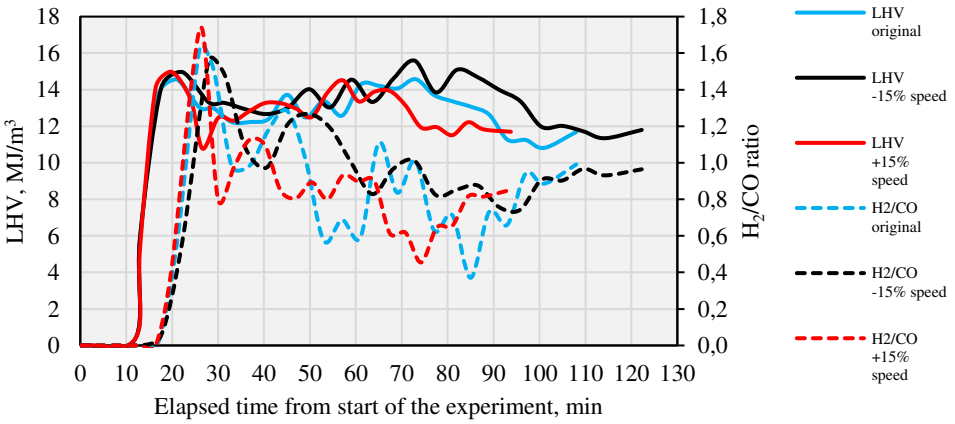

Figure 4

The effect of feeding speed on the LHV and H_2/CO ratio of the gas

Table 5

The average LHV and H_2/CO ratios of the produced gases

Parameter	–15% feeding speed	Original feeding speed	+15% feeding speed
LHV	12.15	11.70	11.49
H_2/CO	0.84	0.76	0.73

The changes of LHV during the experiment *(Figure 4)* revealed that the LHV varied within an approximately ±2 MJ/m^3 interval during the standard feeding speed which is not a substantial deviation for using the syngas for energy purposes. On the other hand, an optimal H_2/CO ratio is necessary to produce a given chemical which would be a challenge to prepare with such a highly fluctuating ratio. Thus, the long-term gas collection and then the modification of the gas composition (H_2 addition) would be necessary for such utilisation.

Considering the total gas quantity *(Table 5)*, the LHV of the gas decreased by the use of a faster feeding speed, even though the amount of hydrocarbons was higher, as stated in *Table 4*. The H_2/CO ratio also decreased with the increasing feeding speed, but the change is not significant. The lowest adequate H_2/CO ratio is 1 and can be used for acetic anhydride and acetic acid production, but all three experiments showed had syngas with lower H_2/CO ratios (0.73–0.84).

CONCLUSION

The aim of this research was to assemble a lab-scale pyrolysis system with continuous operation and study the effect of the feeding speed of raw material during pyrolysis. A laboratory system applicable for both pyrolysis and gasification, with batch and continuous operation was prepared. In the laboratory system, continuous pyrolysis tests were carried out and it was determined that the quantity and composition of the produced gas can be influenced by the feeding speed of the base material.

As the feeding speed was increased, less time was available for the pyrolysis process, decreasing the efficiency of pyrolysis. As there is no time for complete pyrolysis, gas production already starts from the fresh base material during the final phase of the gas production. This way the gas yield can be more stable. On the other hand, as increasing the feeding time results in less time for pyrolysis and lower amount of produced gas with increased amount of hydrocarbons.

Thus, decreasing the feeding speed can result in increased gas yield and a more stable gas composition over time.

Only slight changes were observed in the H_2/CO ratio of the syngas due to the change in feeding speed. However, the ratios themselves was not appropriate for chemical industrial use. The increased feeding speed resulted in slight decrease in the LHV, but based on this value, the gas could be used for energy purposes.

ACKNOWLEDGMENT

The cross-cutting research was conducted at the University of Miskolc as part of the *More efficient exploitation and use of subsurface resources* project implemented in the framework of the Thematic Excellence Program funded by the Ministry of Innovation and Technology of Hungary (Grant Contract reg. nr.: NKFIH-846-8/2019), and within the subsequent *Developments aimed at increasing social benefits deriving from more efficient exploitation and utilization of domestic subsurface natural resources* project supported by the Ministry of Innovation and Technology from the

National Research, Development and Innovation Fund according to the Grant Contract issued by the National Research, Development and Innovation Office (Grant Contract reg. nr.: TKP-17-1/PALY-2020).
The author is grateful to Mária Ambrus for her linguistic advice.

REFERENCES

[1] Gao, F. (2010). Pyrolysis of Waste Plastics into Fuels. PhD dissertation, Chemical and Process Engineering, University of Canterbury.

[2] Singh, A., Biswas, A. K., Singhai, R., Lakaria, B. L., Dubey, A. K. (2015). Effect of Pyrolysis Temperature and Retention Time on Mustard Straw Derived Biochar for Soil Amendment. *J. Basic. Appl. Sci. Res*., Vol. 5 (9), pp. 31–37.

[3] Ningbo, G., Baoling, L., Aimin, L., Juanjuan, L. (2015). Continuous pyrolysis of pine sawdust at different pyrolysis temperatures and solid residence times. *Journal of Analytical and Applied Pyrolysis*, Vol. 114, pp. 155–162, http://doi.org/10.1016/j.jaap.2015.05.011.

[4] Ha, J. H., Lee, I.-G. (2020). Study of a Method to Effectively Remove Char Byproduct Generated from Fast Pyrolysis of Lignocellulosic Biomass in a Bubbling Fluidized Bed Reactor. *Processes*, Vol. 8 (11), 1407, http://doi.org/10.3390/pr8111407.

[5] Hsu, C.-P., Huang, A.-N., Kuo, H.-P. (2015). Analysis of the Rice Husk Pyrolysis Products from a Fluidized Bed Reactor. *Procedia Engineering*, Vol. 102, pp. 1183–1186, http://doi.org/10.1016/j.proeng.2015.01.244.

[6] Newalkar, G., Iisa, K., D'Amico, A. D., Sievers, C., Agrawal, P. (2014). Effect of Temperature, Pressure, and Residence Time on Pyrolysis of Pine in an Entrained Flow Reactor. *Energy & Fuels*, Vol. 28 (8), pp. 5144–5157, http://doi.org/10.1021/ef5009715.

[7] Waldheim, L., Nilsson, T. (2001). *Heating value of gases from biomass gasification. Report prepared for: IEA Bioenergy Agreement, Task 20 - Thermal Gasification of Biomass.* http://www.ieatask33.org/app/webroot/files/file/publications/HeatingValue.pdf (Downloaded: 13. 06. 2021.).

Materials Science and Engineering, Volume 46, No. 1 (2021), pp. 63–69.
http://doi.org/10.32974/mse.2021.007

ANTIOXIDANT POTENTIAL OF BUTYLATED HYDROXYTOLUENE (BHT) – A THEORETICAL STUDY

DALAL K. THBAYH – ANITA RÁGYANSZKI – BÉLA FISER

Abstract: Antioxidants are compounds used to prevent the thermal and photo-oxidative effects of the environment. These molecules are highly important to preserve and prolong various products. A wide variety of synthetic and natural antioxidants applied in the food and polymer industry. A good number of such molecules have phenolic character, such as in the case of butylated hydroxytoluene (BHT) which has various applications. The anti-oxidant potential of BHT has been studied by using the B3LYP density functional theory (DFT) method in combination with the 6-31G(d) basis set in gas phase. Bond dissociation enthalpies (BDEs) have been calculated for each potential hydrogen donor sites (X-H, where X = C or O) of the molecule. The antioxidant potential of the different sites has been compared by using the corresponding BDE values. The calculations indicate that the O-H group has the highest antioxidant potential (lowest BDE value, 290.3 kJ/mol) within BHT. This finding is in good agreement with previous studies. Further calculations are planned to study other antioxidant mechanisms and compounds as well. Based on the current and additional future results, new antioxidant molecules are planned to be proposed and de-signed.

Keywords: BDE, HAT, DFT, phenolic compounds, additives

INTRODUCTION

The properties of polymers depend on several factors. The resistance of a polymeric mate-rial to various conditions such as, sunlight, temperature, humidity, etc. is a fundamental issue which have to be taken into consideration during the synthesis of a product [1]. If the synthesis of the polymeric materials is not carried out carefully, the environmental factors could cause not only esthetic degradation, but potential deterioration of the mechanical properties [2]. Additives are applied to overcome these issues, which are chemicals added to the base polymer to enhance the properties (physical and chemical) of the final product [1]. These compounds are also employed to decrease cost, and maintain aesthetic qualities [3].

Several different additive types are used to enhance specific properties of the polymeric product. Polymer additives are used as plasticizers [e.g., dioctylphthalate (DOP), and tricre-syl phosphate (TCP)], flame retardants [e.g., polybrominated diphenylethers (PBDES), and tris(2-chloroethyI)phosphate (TCEP)], colorants (e.g., anthraquinone, and carbon black), stabilizers (e.g., arium-zinc, and calcium-zinc), antimicrobial agents (e.g., 5-chloro-2-(2,4-dichlorophenoxy)phenol, and 4,5-dichloro-2-noctylisothiazolinone), antioxidants [e.g., butylated hydroxytoluene (BHT), and tert-butylhydroquinone (TBHQ)], and others [4].

To prevent or reduce thermal and photo-oxidative effects antioxidant (AO) additives are applied [1]. Not only polymeric materials are suffering from oxidative stress, but living organisms, and food products as well [5]. For living species, antioxidants can be either endogenous or acquired exogenously like dietary supplements (e.g., BHT) [6]. Enzymatic (e.g., superoxide dismutase) and non-enzymatic antioxidants (e.g., vitamin E, vitamin C) are the two forms of endogenous antioxidants [7].

Free radical scavenging by antioxidants could occur in three different ways, but each of these will lead to the donation of a hydrogen atom (H•) to the free radical. The direct hy-drogen atom (H•) transfer (HAT) to the radical is a one-step mechanism. The other two includes two steps, either first a single electron transfer followed by a proton (H+) transfer (SET-PT), or vice versa, H+ moves first and after the electron (SPLET) from the antioxi-dant to the radical [8]. To study these mechanisms several physical-chemical properties can be measured or computed. Such properties are the bond dissociation enthalpy (BDE), ionization potential (IP), proton dissociation enthalpy (PDE), proton affinity (PA), and electron transfer enthalpy (ETE) [9–12].

Antioxidant molecules can be natural and synthetic compounds [6]. The widespread envi-ronmental issues forced producers to consider replacing commonly used synthetic materi-als with natural alternatives. However, to find environmentally friendly, and effective alternatives of the commonly used additives is difficult to implement and requires a lot of planning and research.

Environmentally friendly antioxidant polymer additives will be proposed and/or designed. Therefore, the antioxidant potential of a widely used food additive, butylated hydroxytol-uene is studied. BHT is extensively used as an additive in the food industry and has been utilized in a variety of food applications [7]. It is also commonly used as a positive control in the measurement of antioxidant activity due to its AO capabilities and simple structure [13, 14]. Our aim is to carry out a theoretical study on the antioxidant activity of various antioxidants *(Figure 1)*, starting with BHT and use the acquired results in AO design in the future.

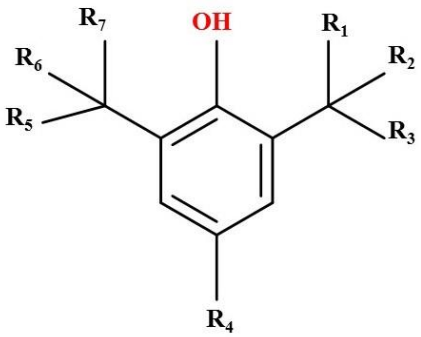

Figure 1
General chemical structure of common antioxidants.

Based on the calculations, new AOs can be designed and later tested as polymer additives to pave the way for a more environmentally friendly polymer composition.

1. MATERIALS AND METHODS

All calculations have been carried out by using the Gaussian 09 program package [15]. The B3LYP density functional theory (DFT) method [16, 17] in combination with the 6-31G(d) basis set has been used to optimize the studied molecule and the corresponding radical species in gas phase. The bond dissociation enthalpies (BDE) of each potential hydrogen donor sites of the molecule have been computed by considering the following hypothetical reaction:

$$A \rightarrow A\bullet + H\bullet$$

where 'A' is the antioxidant molecule, while A• and H• are the corresponding radical and hydrogen atom which will form after the dissociation of an X-H (X = C, or O) bond.

2. RESULTS AND DISCUSSION

Direct hydrogen atom (H•) transfer (HAT) mechanism is considered. In this case, the mole-cule donates a hydrogen atom to the free radical and thus, the reactive compound is neu-tralized. To compare the antioxidant activity of the different groups, bond dissociation enthalpies (BDEs) have been calculated for each potential hydrogen donor sites (X-H, where X = C, or O) of the molecule. The different sites have been compared by using the corresponding BDE values. The bond lengths vary between 0.964 Å and 1.097 Å within the optimized structure of the molecule *(Figure 2).*

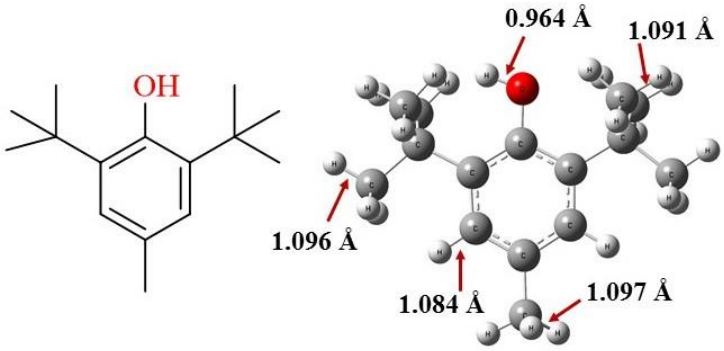

Figure 2

2D and 3D structure of butylated hydroxytoluene (BHT). The 3D structure has been opti-mized at the B3LYP/6-31G(d) level of theory in gas phase. The corresponding bond lengths are also depicted.

The radicals were prepared from the optimized BHT molecule by removing one hydrogen atom from each potential sites *(Figure 3)*. All in all, six radicals have been created and the structures have been optimized *(Figure 3)*.

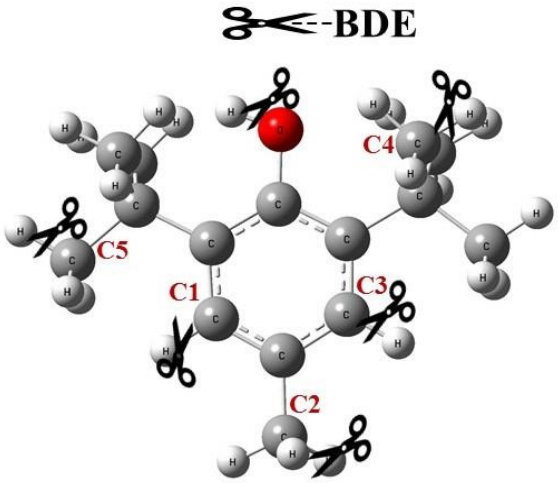

Figure 3
Hydrogen atom donor sites of butylated hydroxytoluene (BHT)

By using the computed thermodynamic properties of BHT and the corresponding radicals, BDE values of the functional groups have been computed along with zero-point corrected relative energies (DE0) and relative Gibbs free energies (DG) according to the above-mentioned hypothetical reaction (see Materials and Methods and *Table 1*).

Table 1
Bond Dissociation enthalpies (BDEs) of butylated hydroxytoluene (BHT), zero-point cor-rected relative energies (DE0), and relative Gibbs free energies (DG). All structures have been computed at the B3LYP/6-31G(d) level of theory in gas phase

X-H position	ΔE_0	ΔG	BDE	Bond length
	kJ/mol			Å
O-H	285.1	254.7	290.3	0.964
C1-H	443.0	412.3	449.6	1.084
C2-H	358.4	332.3	363.2	1.097
C3-H	443.0	412.3	449.6	1.084
C4-H	390.4	361.7	395.8	1.091
C5-H	411.9	380.4	419.5	1.096

The BDEs of the C-H bonds within BHT cover a wide range starting from 363.2 and reach-ing to 449.6 kJ/mol *(Table 1, Figure 4)*. The weakest within the C-H bonds is C2-H (1.097 Å) and it is located on the methyl group which is in the para position and has a BDE of 363.2 kJ/mol *(Figure 4)*. The removal of a hydrogen atom from the aromatic ring of BHT is unfavourable as the strongest bonds are C1-H and C3-H (1.084 Å), which have identical BDE values (449.6 kJ/mol). The results indicate that

shorter bond length can be associated with larger bond dissociation enthalpy and thus, stronger bond. All in all, the BDE values indicate that the O-H is the weakest (290.3 kJ/mol) within the studied set of bonds *(Table 1, Figure 4)*. This finding is in good agreement with previous studies [7].

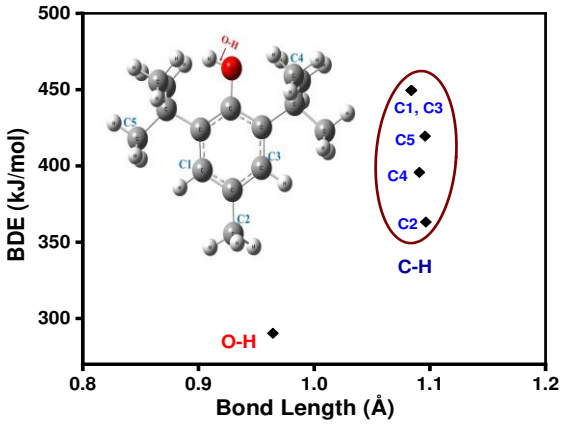

Figure 4

Bond dissociation enthalpy (BDE) vs. bond length diagram of butylated hydroxytoluene (BHT). All structures have been computed at the B3LYP/6-31G(d) level of theory in gas phase.

The lower the BDE value, higher the ability of the antioxidant to donate its hydrogen atom to free radicals. Thus, based on these results, it is obvious that the hydroxyl group contrib-utes mostly to the antioxidant activity of BHT compared to C-H bonds when the HAT mechanism is considered. However, C-H bonds (e.g., C2-H) can also play a role in the antioxidant process and thus, the antioxidant potential of BHT is significant.

CONCLUSION

The antioxidant potential of butylated hydroxytoluene (BHT) have been studied by using computational chemical tools and considering the direct hydrogen atom (H•) transfer (HAT) mechanism. To reveal the antioxidant activity of the different groups, bond disso-ciation enthalpies (BDEs) have been calculated for each potential hydro-gen donor sites of the molecule. All in all, seven potential hydrogen donor sites were considered, and their BDE values were compared.

The weakest within the C-H bonds is located on the methyl group which is in the para posi-tion and has a BDE of 363.2 kJ/mol. The removal of a hydrogen atom from the aromatic ring of BHT is unfavourable as the strongest C-H bonds indicates (449.6 kJ/mol). All in all, the O-H is the weakest (290.3 kJ/mol) within the studied set of bonds and thus, the hy-droxyl group contributes mostly to the antioxidant activity of BHT when the HAT mecha-nism is considered. However, C-H bonds can also play a role in the antioxidant process and thus, the antioxidant potential of BHT is signifi-

cant. Additional calculations are planned to study the performance of BHT in other antioxidant mechanisms (SET-PT and SPLET). Furthermore, additional molecules will also be studied to explore their potential application as antioxidant additives in polymer synthesis. Based on the current and future results, new AO additives are planned to be proposed and designed.

ACKNOWLEDGEMENTS

This research is supported by the European Union and the Hungarian State, co-financed by the European Regional Development Fund in the framework of the GINOP-2.3.4-15-2016-00004 project, which aimed to promote the cooperation between the higher education and the industry. BF thanks the support by the ÚNKP-20-4 New National Excellence Program of The Ministry for Innovation and Technology from the source of the National Research, Development, and Innovation Fund (Hungary). The GITDA (Governmental Information-Technology Development Agency, Hungary) is gratefully acknowledged for allocating computing resources used in this work.

REFERENCES

[1] Ambrogi, V., Carfagna, C., Cerruti, P., Marturano, V. (2017). Additives in polymers. In: *Modification of Polymer Properties*. Jasso-Gastinel, C. F., Kenny, J. M. (eds.), Cambridge: Elsevier, pp. 87–108, http://doi.org/1016/B978-0-323-44353-1.00004-X.

[2] Kockott, D. (1989). Natural and artificial weathering of polymers. *Polymer Degradation and Stability*, Vol. 25, No. 2–4, pp. 181–208, http://doi.org/10.1016/S0141-3910(89)81007-9.

[3] Calzonetti, J. A., Laursen, C. J. (2010). Patents of Charles Goodyear: His international contributions to the rubber industry. *Rubber Chemistry and Technology*, Vol. 83, No. 3, pp. 303–321, http://doi.org/10.5254/1.3525687.

[4] Paoli, M. A. D., Waldman, W. R. (2019). Bio-based additives for thermoplastics. *Polímeros*, Vol. 29, No. 2, e2019030, http://doi.org/10.1590/0104-1428.06318.

[5] Rezaeisadat, M., Bordbar, A.-K., Omidyan, R. (2021). Molecular dynamics simula-tion study of curcumin interaction with nano-micelle of PNIPAAm-b-PEG co-polymer as a smart efficient drug delivery system. *Journal of Molecular Liquids*, Vol. 332, p. 115862, http://doi.org/10.1016/j.molliq.2021.115862.

[6] Neha, K., Haider, M. R., Pathak, A., Yar, M. S. (2019). Medicinal prospects of antioxi-dants: A review. *European Journal of Medicinal Chemistry*, Vol. 178, pp. 687–704, http://doi.org/10.1016/j.ejmech.2019.06.010.

[7] Boulebd, H. (2020). Comparative study of the radical scavenging behavior of ascorbic acid, BHT, BHA and Trolox: experimental and theoretical study. *Journal of Molecular Struc*ture, vol. 1201, p. 127210, http://doi.org/10.1016/j.molstruc.2019.127210.

[8] Najafi, M., Zahedi, M., Klein, E. (2011). DFT/B3LYP study of the solvent effect on the reaction enthalpies of homolytic and heterolytic OH bond cleavage in mono-substituted chromans. *Computational and Theoretical Chemistry*, Vol. 978, No. 1–3, pp. 16–28, http://doi.org/10.1016/j.comptc.2011.09.014.

[9] Wang, L., Yang, F., Zhao, X., Li, Y. (2019). Effects of nitro-and amino-group on the antioxidant activity of genistein: a theoretical study. *Food Chemistry*, Vol. 275, pp. 339–345.

[10] Rimarčík, J., Lukeš, V., Klein, E., Ilčin, M. (2010). Study of the solvent effect on the enthalpies of homolytic and heterolytic N–H bond cleavage in p-phenylenediamine and tetracyano-p-phenylenediamine. *Journal of Molecular Structure: Theochem*, Vol. 952, No. 1–3, pp. 25–30, http://doi.org/10.1016/j.theochem.2010.04.002.

[11] Thong, N. M., Duong, T., Pham, L. T., Nam, P. C. (2014). Theoretical investigation on the bond dissociation enthalpies of phenolic compounds extracted from Artocarpus altilis using ONIOM (ROB3LYP/6-311++ G (2df, 2p): PM6) method. *Chemical Physics Letters*, Vol. 613, pp. 139–145, http://doi.org/10.1016/j.cplett.2014.08.067.

[12] Thong, N. M., Quang, D. T., Bui, N. H. T., Dao, D. Q., Nam, P. C. (2015). Antioxidant properties of xanthones extracted from the pericarp of Garcinia mangostana (Mango-steen): a theoretical study. *Chemical Physics Letters*, Vol. 625, pp. 30–35, http://doi.org/10.1016/j.cplett.2015.02.033.

[13] Moon, J.-K., Shibamoto, T. (2009). Antioxidant assays for plant and food compo-nents. *Journal of Agricultural and Food Chemistry*, Vol. 57, No. 5, pp. 1655–1666, http://doi.org/10.1021/jf803537k.

[14] Brand-Williams, W., Cuvelier, M.-E., Berset, C. (1995). Use of a free radical method to evaluate antioxidant activity. *LWT-Food Science and Technology*, Vol. 28, No. 1, pp. 25–30, http://doi.org/10.1016/S0023-6438(95)80008-5.

[15] Frisch, M. J., Trucks, G., Schlegel, H. B., Scuseria, G., Robb, M., Cheeseman, J., Scalmani, G. V. B., Mennucci, B., Petersson, G. (2009). *Gaussian 09, revision A. 1*. Gaussian Inc., Walling-ford Ct, 27, 34.

[16] Becke, A. D. (1988). Density-functional exchange-energy approximation with correct asymptotic behavior. *Physical Review A*, Vol. 38, No. 6, p. 3098, http://doi.org/10.1103/PhysRevA.38.3098.

[17] Beck, A. D. (1993). Density-functional thermochemistry. III. The role of exact ex-change. *Journal Chemistry Physics*, Vol. 98, No. 7, pp. 5648-6, http://doi.org/10.1063/1.464913.

Materials Science and Engineering, Volume 46, No. 1 (2021), pp. 70–77.
http://doi.org/10.32974/mse.2021.008

THE CATALYTIC EFFECT OF DBU ON URETHANE FORMATION – A COMPUTATIONAL STUDY

HADEER Q. WALEED[1] – MARCELL CSÉCSI[2] – RACHID HADJADJ[3] – RAVIKUMAR THANGARAJ[4] – MICHAEL OWEN[5] –MILÁN SZŐRI[6] – ZSOLT FEJES[7] – BÉLA VISKOLCZ[8] – BÉLA FISER[9]

Abstract: A theoretical investigation of urethane formation through the reaction of phenyl isocyanate and methanol without and in the presence of a secondary ketimine catalyst (DBU) was carried out by using density functional theory method in gas phase and in organic solvent (THF). The reaction mechanisms have been explored, and the corresponding thermodynamic properties have been computed. The reaction in the presence of the catalyst largely differs from the catalyst-free case. It was found that the activation energy decreased significantly in the presence of DBU in both gas phase and organic solvent by more than 67.0 kJ/mol, compared to the catalyst-free reaction, which proves the importance of catalysts in (poly)urethane synthesis.

Keywords: Polyurethane, DFT, Secondary ketimine, THF, Catalyst-free

INTRODUCTION

The term catalysis was coined by Berzelius in 1835 and comes from the Greek words "kata" meaning down and "lyein" meaning loosen [1], [2]. Catalysts are key in the

[1] Institute of Chemistry, University of Miskolc, 3515 Miskolc-Egyetemváros, Hungary
kemhader@uni-miskolc.hu
[2] Institute of Chemistry, University of Miskolc, 3515 Miskolc-Egyetemváros, Hungary
csecsi.marcell2@gmail.com
[3] Institute of Chemistry, University of Miskolc, 3515 Miskolc-Egyetemváros, Hungary
hrachid.chemeng@gmail.com
[4] Institute of Chemistry, University of Miskolc, 3515 Miskolc-Egyetemváros, Hungary
ravikumar8019@gmail.com
[5] Institute of Chemistry, University of Miskolc, 3515 Miskolc-Egyetemváros, Hungary
michaelowen27@gmail.com
[6] Institute of Chemistry, University of Miskolc, 3515 Miskolc-Egyetemváros, Hungary
kemszori@uni-miskolc.hu
[7] Institute of Chemistry, University of Miskolc, 3515 Miskolc-Egyetemváros, Hungary
kemfejes@uni-miskolc.hu
[8] Institute of Chemistry, University of Miskolc, 3515 Miskolc-Egyetemváros, Hungary
bela.viskolcz@uni-miskolc.hu
[9] Institute of Chemistry, University of Miskolc, 3515 Miskolc-Egyetemváros, Hungary
Higher Education and Industrial Cooperation Centre, University of Miskolc, 3515 Miskolc-Egyetemváros, Hungary
Ferenc Rákóczi II. Transcarpathian Hungarian College of Higher Education, 90200 Beregszász, Transcarpathia, Ukraine, kemfiser@uni-miskolc.hu

chemical industry and with their help the environmental impact of chemical processes and the energy required to carry them out are significantly reduced [3]. Catalysts can expedite chemical reactions compared to catalyst-free systems. By applying catalysts, new reaction pathways may become possible [4]. Currently, catalysts are used in more than 90% of chemical and refining processes. The world depends on them, as plastics, artificial fibres, food, and fuel are prepared by using these special chemicals [5]. Also, catalysts are important additives in the process of synthesizing polymers, especially in polyurethane (PU) synthesis [6]. PU is one of the most versatile and unique polymer being a part of our daily life and used in different applications [7]. Therefore, there are various types of catalysts used for polyurethane synthesis. The PU catalyst can increase the reaction rate, the production efficiency, and promote the urethane formation while suppress the side reactions selectively [8]. In the production of polyurethane-based products, although the amount of catalyst is small, but its role is significant. The most important catalysts applied in PU foam production are amine-containing chemicals [8].

The reaction between methyl isocyanate and methanol with and without catalyst addition has been studied at the B3LYP/3-21G level of theory. It was found that the addition of the catalysts has a great influence on the stability of the transition states [9]. However, there are still various aspects of the catalytic urethane formation reactions which has to be understood. There is also an increasing demand to design environmentally friendly polyurethane catalysts. Therefore, additional studies to gain more information about urethane and polyurethane synthesis is inevitable.

In the current work, urethane formation is studied by using computational chemical tools in the presence of a secondary ketimine catalyst, 1,8-diazabicyclo [5.4.0]undec-7-ene (DBU). The effect of the catalyst on the phenyl isocyanate – methanol reaction is examined, and the steps of the reaction are described.

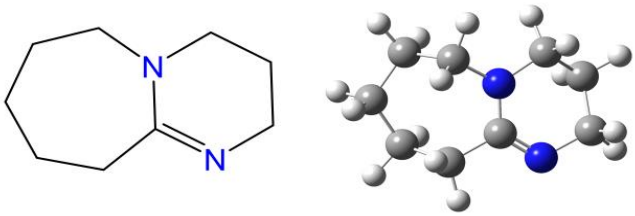

Figure 1
2D and 3D structures of the studied catalyst, 1,8-diazabicyclo [5.4.0]undec-7-ene (DBU)

1. METHODS

All calculations were performed by using the B3LYP (Becke, 3-parameter, Lee-Yang-Parr) [10] DFT method in combination with the 6-31G(d) basis set in gas phase, and in tetrahydrofuran (THF, $\varepsilon_r = 7.4257$) by using the SMD implicit solvent model. Opti-

mizations and frequency calculations were carried out to locate the minima and transition states. Intrinsic reaction coordinate (IRC) calculations were also performed starting from the transition states to verify that those connect the right minima. The Gaussian 09 program package was used to carry out the calculations [11].

2. RESULTS AND DISCUSSION

2.1. Catalyst-free Reaction between Phenyl Isocyanate and Methanol

The methanol (MeOH) - phenyl isocyanate (PhNCO) reaction has been used as a model to study urethane formation. For the catalyst-free system, the geometries have been optimized in gas phase and THF, and the corresponding thermodynamic properties have been computed *(Table 1)*, and based on these, the reaction has been characterized *(Figure 2)*.

Table 1

The zero-point corrected relative energies (ΔE_0), enthalpies (ΔH), and Gibbs free energies (ΔG) of the reaction between phenyl isocyanate (PhNCO) and methanol with and without catalyst (DBU), calculated at the B3LYP/6-31G(d) level of theory in gas phase and THF at 298.15 K and 1 atm. R: reactants, RC: reactant complex, TS: transition state, IM: intermediate, PC: product complex, P: product

Catalyst-free	**ΔE_0 (kJ/mol)**		**ΔH (kJ/mol)**		**ΔG (kJ/mol)**	
	Gas	**THF**	**Gas**	**THF**	**Gas**	**THF**
R (PhNCO+MeOH)	0.00	0.00	0.00	0.00	0.00	0.00
RC	–15.81	–10.40	–14.15	–8.92	20.85	27.24
TS	107.93	110.22	104.79	106.85	156.35	159.14
P	–100.38	–100.32	–103.70	–103.57	–51.43	–54.37
Catalysed	**ΔE_0 (kJ/mol)**		**ΔH (kJ/mol)**		**ΔG (kJ/mol)**	
	Gas	**THF**	**Gas**	**THF**	**Gas**	**THF**
R (PhNCO+MeOH+DBU)	0.00	0.00	0.00	0.00	0.00	0.00
RC	–66.03	–39.66	–62.66	–35.62	18.34	41.53
TS1	–9.69	–8.04	–11.31	–9.09	84.65	85.76
IM	–37.49	–102.89	–39.50	–104.60	63.69	–7.03
TS2	–*	–108.68	–*	–111.17	–*	–10.37
PC	–140.84	–129.74	–142.01	–130.86	–45.86	–36.00
P	–100.38	–100.32	–103.70	–103.57	–51.43	–54.37

* – TS2 were not found in gas phase.

It can be seen from the optimized geometries that the urethane bond formation is going through a concerted mechanism *(Figure 2)*. It starts with the formation of the reactant complex (RC, PhNCO---MeOH). The geometrical properties of the complex in gas phase and THF are slightly differ (2.179 and 2.150 Å, respectively) *(Figure 2)*.

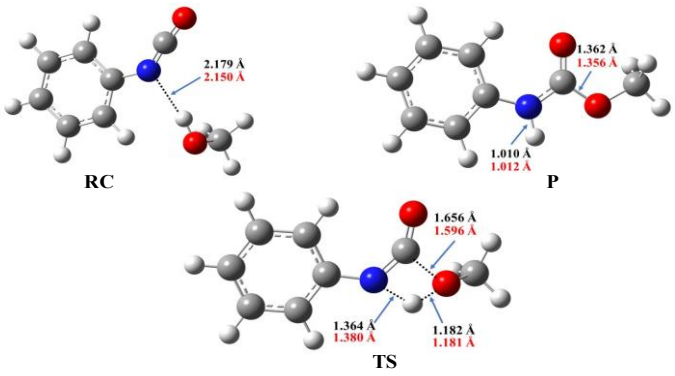

Figure 2

3D structures in the reaction of phenyl isocyanate (PhNCO) and methanol. The optimizations were carried out at the B3LYP/6-31G(d) level of theory in gas and solvent (THF) phase at 298.15 K and 1 atm. RC: reaction complex, TS: transition state, and P: product. The most important distances are also depicted in Å. Black: gas phase. Red: THF.

The corresponding zero-point corrected relative energy, enthalpy and Gibbs free energy values indicates that the complex is more stable in gas phase than in THF. In the next step, the product (P) will be formed through the transition state (TS). In the TS, a proton transfer from the methanol's hydroxyl group to the isocyanate's nitrogen will occur and a bond will be formed between the oxygen of the methanol and the carbon of the isocyanate group. The N-H distance in the TS is 1.364 Å, and 1.380 Å in gas phase and in THF, respectively. The forming C-O bond in the TS between the isocyanate's carbon and methanol's oxygen is 1.656 Å, and 1.596 Å in gas phase and in THF, respectively. The TS has the highest relative energy along the reaction pathway and a significant barrier height has to be overcome to achieve the product *(Figure 3)*.

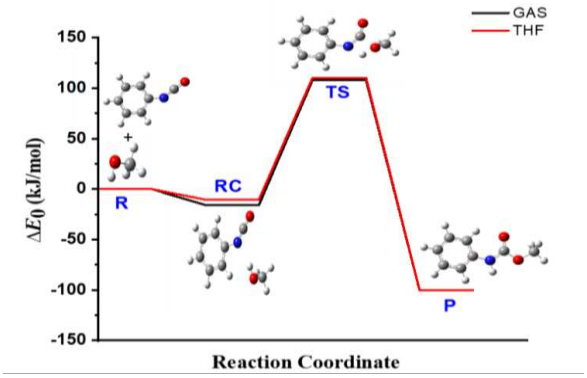

Figure 3

Energy diagram (zero-point corrected) of the phenyl isocyanate (PhNCO) and methanol reaction calculated at the B3LYP/6-31G(d) level of theory in gas phase and THF (using the SMD implicit solvent model) at 298.15 K and 1 atm

The zero-point corrected relative energies indicate that the final urethane product, P is very stable and the corresponding DE_0 is –100.3 kJ/mol *(Table 1)*.

2.2. Reaction between Phenyl Isocyanate and Methanol in the Presence of DBU

The steps of the phenyl isocyanate – methanol reaction in the presence of the DBU catalyst in gas phase and THF has also been computed *(Figure 4, Table 1)*. Additional structures (e.g., IM) have been formed compared to the catalyst-free pathway.

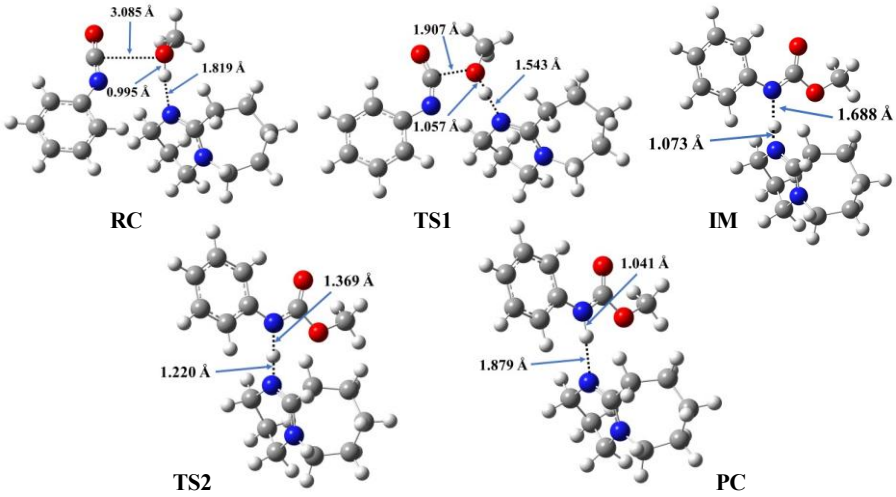

Figure 4

3D structures of the reaction between phenyl isocyanate (PhNCO) and methanol in the presence of DBU. The structures have been optimized at the B3LYP/6-31G(d) level of theory in THF at 298.15 K and 1 atm. RC: reaction complex, TS: transition state, IM: intermediate, PC: product complex. The bond distances are also depicted in Å.

In the first step, a trimolecular reactant complex, RC was formed in this case. A hydrogen bond formed between the hydroxyl group of the methanol and the DBU's nitrogen and the corresponding N-H distance is 1.799 Å, and 1.819 Å in gas phase and THF, respectively *(Figure 4)*. Another interaction established between the isocyanate's carbon and methanol's hydroxyl oxygen. The C-O distance is slightly longer in gas phase (3.183 Å) than in THF (3.085 Å). The reaction is going through two transition states and an intermediate. After the formation of the complex (RC), a proton transfer will occur in TS1 from the hydrogen of the hydroxyl group to the nitrogen of the catalyst and thus, the N-H distance will be reduced (N-H_{gas} = 1.410 Å, and N-H_{THF} = 1.543 Å) compared to that of the reaction complex. Furthermore, a bond is forming between the methanol's oxygen and the isocyanate's carbon. The relative energy of the TS1 is lower than the reactants' level (ΔE_{0gas} = –9.69 kJ/mol,

and $\Delta E_{0THF} = -8.04$ kJ/mol) *(Table 2, Figure 5)*. This is a significant decrease compared to the catalyst-free case. On the other hand, the solvent has only a slight effect on the relative energy of TS1 ($\Delta E_{0gas\text{-}THF} = 1.65$ kJ/mol).

Through TS1, an intermediate structure (IM) obtained within which a bond is formed between the isocyanate's carbon and the methanol's oxygen, while the protonated DBU is hydrogen bonded to the nitrogen of the former isocyanate group *(Figure 4)*. The relative stability of the IM in gas and solvent phase differs significantly ($DDE_{0gas\text{-}THF} = 65.4$ kJ/mol).

The reaction was continued with TS2 within which the proton transfer from the catalyst to the product will occur. It can be seen that in TS2 one N-H distance decreased, while the other increase compared to the IM *(Figure 4)*. The zero-point corrected relative energy of TS2 calculated in THF is -108.68 kJ/mol, which is slightly lower than in the case of IM ($DE_0 = -102.89$ kJ/mol) *(Table 1, Figure 5)*. Due to the potential limitations of the method, attempts to locate TS2 were not successful in gas phase. The penultimate step in this reaction mechanism is the formation of the product complex (PC). It is a bimolecular complex of the final product methyl phenylcarbamate and DBU *(Figure 4)*. The final step is the separation of the catalyst from the product. All in all, the solvent has a quite large effect on the energetics of the catalytic reaction *(Table 1)*. The presence of the catalyst changes significantly the reaction mechanism compared to the catalyst-free case. The product will form through a multi-step pathway and the relative energies are also significantly reduced by the presence of DBU *(Figure 3 and Figure 5)*.

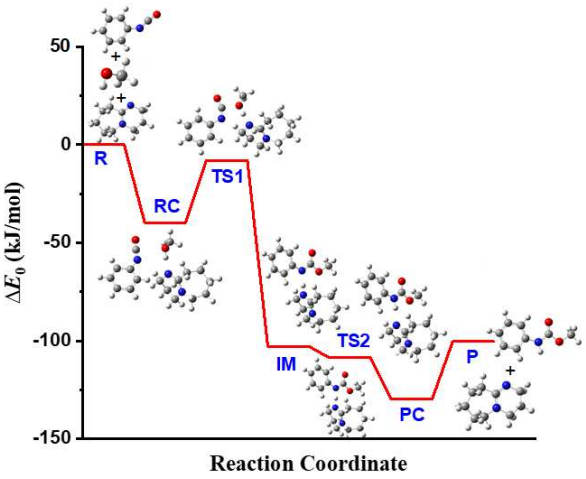

Figure 5

Energy diagram (zero-point corrected) of the phenyl isocyanate (PhNCO) and methanol reaction in the presence of DBU calculated at the B3LYP/6-31G(d) level of theory in THF using the SMD implicit solvent model at 298.15 K and 1 atm. R: reactants+catalyst (PhNCO+MeOH+DBU), RC: reactant complex, TS: transition state, IM: intermediate, PC: product complex, P: product

CONCLUSION

Catalysts play a fundamental role in industrial chemical transformations. Most of the chemicals are made through catalytic processes since catalysts provide energetically more favorable reaction pathways compared to noncatalytic processes. The urethane formation between phenyl isocyanate and methanol as a model system in the presence of a secondary ketimine (DBU) catalyst was investigated. Using DFT calculation at the B3LYP/6-31G(d) level of theory the reaction was investigated in gas phase and in organic solvent (THF). The catalyst-free reaction was also computed and used as a reference. The results showed that the highest energy point along the reaction in the presence of DBU was below the entrance level ($\Delta E_{0gas} = -9.69$ kJ/mol, and $\Delta E_{0THF} = -8.04$ kJ/mol), while the corresponding value in the catalyst-free case was above 100 kJ/mol in both gas phase and THF ($\Delta E_{0gas} = 107.93$ kJ/mol, and $\Delta E_{0THF} = 110.22$ kJ/mol). Thus, by adding a catalyst to the system, the activation energy is significantly reduced, and urethane formation is promoted. A multi-step catalytic process revealed, and further studies will be carried out to understand other aspects of the reaction. Based on the current and upcoming results, the design of new catalysts will be possible in the near future.

ACKNOWLEDGMENT

This research is supported by the European Union and the Hungarian State, co-financed by the European Regional Development Fund in the framework of the GINOP-2.3.4-15-2016-00004 project, which aimed to promote the cooperation between the higher education and the industry. BF thanks the support by the ÚNKP-20-4 New National Excellence Program of The Ministry for Innovation and Technology from the source of the National Research, Development, and Innovation Fund (Hungary). The GITDA (Governmental Information-Technology Development Agency, Hungary) is gratefully acknowledged for allocating computing resources used in this work.

REFERENCES

[1] Wisniak, J. (2010). The History of Catalysis. From the Beginning to Nobel Prizes. *Educuation Chimcia*, Vol. 21, No. 1, pp. 60–69, http://doi.org/10.1016/S0187-893X(18)30074-0

[2] Yanping, Y. (2018). The development of polyurethane. *Mater. Sci. Mater. Rev.*, Vol. 1, No. 1, pp. 1–8, http://doi.org/10.18063/msmr.v1i1.507.

[3] Silva, A. L., Bordado, J. C. (2004). Recent developments in polyurethane catalysis: Catalytic mechanisms review. *Catal. Rev. – Sci. Eng.*, Vol. 46, No. 1, pp. 31–51, http://doi.org/10.1081/CR-120027049.

[4] Gates, B. C., Huber, G. W., Marshall, C. L., Ross, P. N., Siirola, J., Wang, Y. (2008). Catalysts for emerging energy applications. *MRS Bull.*, Vol. 33, No. 4, pp. 429–435, http://doi.org/10.1557/mrs2008.85.

[5] Lloyd, L. (2008). *Handbook of industrial catalysts*. New York, NY, USA: Springer.

[6] Dworakowska, S., Bogdał, D., Zaccheria, F., Ravasio, N. (2014). The role of catalysis in the synthesis of polyurethane foams based on renewable raw materials. *Catal. Today*, Vol. 223, pp. 148–156, http://doi.org/10.1016/j.cattod.2013.11.054.

[7] Cavaco, L. I. (2012). *Polyurethanes properies, structure and applications*. New York: Nova Science Publishers, Inc.

[8] Ruiduan, L., Ling, L., Yanjie, L., Ben, W., Jia Jun, Y., Jibo, Z. (2018). Research Progress of Amine Catalysts for Polyurethane. Vol. 1, No. 1, pp. 54–57, http://doi.org/10.26480/icnmim.01.2018.54.57.

[9] Hatanaka, M. (1993). DFT Analysis of Catalytic Urethanation. *Bull. Chem. Soc. Jpn.*, Vol. 84, No. 9, pp. 933–935, http://doi.org/10.1246/bcsj.20110144.

[10] Becke, A. D. (1993). Density-functional thermochemistry. III. The role of exact exchange. *J. Chem. Phys.*, Vol. 98, No. 7, pp. 5648–5652, http://doi.org/10.1063/1.464913.

[11] Frisch, M. J., Trucks, G. W., Schlegel, H. B., Scuseria, G. E., Robb, M. A., Cheeseman, J. R., Scalmani, G., Barone, V., Menucci, B., Petersson G. A. et al. (2009). *Gaussian 09, Revision, E.01*. Gaussian, Inc.: Wallingford, CT, USA.